AUTHOR

Ana Figueiredo, Sonia Trikha Rastogi, Susana Ramos, Fátima Nogueira, Katherine De Villiers, António G. Gonçalves de Sousa, Lasse Votborg-Novél, Cäcilie von Wedel, Pinkus Tober-Lau, Elisa Jentho, Sara Pagnotta, Miguel Mesquita, Silvia Cardoso, Giulia Bortolussi, Andrés F. Muro, Erin M. Tranfield, Jessica Thibaud, Denise Duarte, Ana Laura Sousa, Sandra N. Pinto, Jamil Kitoko, Ghyslain Mombo-Ngoma, Johannes Mischlinger, Sini Junttila, Marta Alenquer, Maria João Amorim, Chirag Vasavda, Piter J. Bosma, Sara Violante, Bernhard Drotleff, Tiago Paixão, Silvia Portugal, Florian Kurth, Laura L. Elo, Bindu D. Paul, Rui Martins, and Miguel P. Soares

TITLE

A metabolite-based resistance mechanism against malaria

YEAR

2025

DOI

https://doi.org/10.1126/science.adq6741

VERSION

Author's accepted manuscript

CITATION

Ana Figueiredo et al., A metabolite-based resistance mechanism against malaria. Science 388, eadq6741 (2025). DOI: 10.1126/science.adq6741

A Metabolite-Based Resistance Mechanism Against Malaria

Ana Figueiredo[1], Sonia Trikha Rastogi[1*], Susana Ramos[1*], Fátima Nogueira[2*], Katherine De Villiers[3], António G. Gonçalves de Sousa[4], Lasse Votborg-Novél[5], Cäcilie von Wedel[6,7], Pinkus Tober-Lau[6], Elisa Jentho[1,8], Sara Pagnotta[1], Miguel Mesquita[1], Silvia Cardoso[1], Giulia Bortolussi[9], Andrés F. Muro[9], Erin M. Tranfield[1,10], Jessica Thibaud[3], Denise Duarte[2], Ana Laura Sousa[1], Sandra N. Pinto[11], Jamil Kitoko[1], Ghyslain Mombo-Ngoma[7,12], Johannes Mischlinger[7,12], Sini Junttila[4], Marta Alenquer[13], Maria João Amorim[13], Chirag Vasavda[14,15], Piter J. Bosma[16], Sara Violante[1], Bernhard Drotleff[17], Tiago Paixão[1], Silvia Portugal[5], Florian Kurth[6,7], Laura L. Elo[4,18], Bindu D. Paul[14,19,20,21], Rui Martins[1] & Miguel P. Soares[1**]

[1]Gulbenkian Institute for Molecular Medicine (GIMM), Avenida Professor Egas Moniz 1649-035 Lisboa, Portugal.

[2]Global Health and Tropical Medicine, Instituto de Higiene e Medicina Tropical, IHMT, Universidade NOVA de Lisboa, Rua da Junqueira 100, 1349-008 Lisboa, Portugal.

[3]Department of Chemistry and Polymer Science, Stellenbosch University, South Africa.

[4]Turku Bioscience Centre, University of Turku and Åbo Akademi University, Tykistökatu 6, 20520 Turku, Finland.

[5]Max Planck Institute for Infection Biology, 10117 Berlin, Germany.

[6]Department of Infectious Diseases and Intensive Care Medicine, Charité Universitätsmedizin Berlin, Corporate Member of Freie Universität Berlin and Humboldt-Universität zu Berlin, 13353 Berlin, Germany.

[7]Centre de Recherches Médicales de Lambaréné, Lambaréné, Gabon.

[8]Department of Anesthesiology and Intensive Care Medicine, Jena University Hospital, Friedrich-Schiller-University, Jena, Germany.

[9]International Centre for Genetic Engineering and Biotechnology Padriciano 99 34149 Trieste, Italy.

[10]Current address: VIB-UGent Center for Inflammation Research, Technologiepark-Zwijnaarde 71, 9052 Ghent, Belgium

[11]iBB-Institute for Bioengineering and Biosciences and i4HB-Institute for Health and Bioeconomy, Instituto Superior Técnico, Av. Rovisco Pais, 1049-001 Lisboa, Portugal.

[12]Bernhard Nocht Institute for Tropical Medicine & I. Dept. of Medicine, University Medical Center Hamburg-Eppendorf, Hamburg, Germany.

[13]Católica Biomedical Research Centre (CBR), Católica Medical School - Universidade Católica Portuguesa, Palma de Cima, 1649-023, Lisboa, Portugal.

[14]The Solomon H. Snyder Department of Neuroscience, Johns Hopkins University School of Medicine, Baltimore, MD 21205, USA.

[15]Current address: Department of Dermatology, Brigham and Women's Hospital, Boston, MA, USA, Harvard Medical School, Boston, MA

[16]Amsterdam UMC, University of Amsterdam, Tytgat Institute for Liver and Intestinal Research, AG&M, Meibergdreef 69-71, 1105 BK Amsterdam, the Netherlands.

[17]Metabolomics Core Facility, European Molecular Biology Laboratory, Heidelberg, Germany

[18]Institute of Biomedicine, University of Turku, 20520 Turku, Finland.

[19]Department of Pharmacology and Molecular Sciences, Johns Hopkins University School of Medicine, Baltimore, MD 21205, USA.

[20]Department of Psychiatry and Behavioral Sciences, Johns Hopkins University School of Medicine, Baltimore, MD 21205, USA.

[21]Lieber Institute for Brain Development, Baltimore, MD 21205, USA.

*Equal contribution **Corresponding author (miguel.soares@gimm.pt)

Abstract

Jaundice is a common presentation of *Plasmodium* (*P.*) *falciparum* malaria (*1-3*), arising from the accumulation of circulating bilirubin. We do not understand whether it represents an adaptive or maladaptive response to *Plasmodium* spp. infection (*1-3*). We found that asymptomatic *P. falciparum* infection was associated with a higher ratio of unconjugated over conjugated bilirubin and parasite burden, compared to symptomatic malaria. Genetic suppression of bilirubin synthesis by biliverdin reductase A (BVRA) (*4*) increased parasite virulence and malaria mortality in mice. Accumulation of unconjugated bilirubin in plasma, via genetic inhibition of hepatic conjugation by UDP glucuronosyltransferase family 1 member A1 (UGT1A1) (*5*), was protective against malaria in mice. Unconjugated bilirubin inhibited *P. falciparum* proliferation in red blood cells (RBC) by a mechanism that suppressed mitochondrial pyrimidine synthesis. Moreover, unconjugated bilirubin inhibited hemozoin (Hz) crystallization and compromised the parasite´s food vacuole. Hence, jaundice appears to represent a metabolic response to *Plasmodium* spp. infection that limits malaria severity.

Introduction

Parasites from the *Plasmodium* genus proliferate in the red blood cell (RBC) compartment of their numerous vertebrate hosts leading to intravascular hemolysis and release of hemoglobin into plasma (*6, 7*). Auto-oxidation of extracellular hemoglobin precipitates the detachment of its non-covalently bound prosthetic heme groups (*6, 8-11*). This produces labile heme (*12*), an independent risk factor for *P. falciparum* malaria severity partaking in the pathogenesis of severe malaria in mice (*8, 10, 13*).

The pathogenic effects of labile heme are countered by heme oxygenase-1 (HO-1/*HMOX1*) (*8, 9, 14*). This stress-responsive enzyme catabolizes heme into biliverdin (*15*), which is reduced into lipophilic bilirubin, by biliverdin reductase A (BVRA) (*4*) (*Fig. S1A*). Unconjugated bilirubin circulates in plasma bound to albumin (*16*) (*Fig. S1A*) and is conjugated to glucuronic acid by UDP glucuronosyltransferase family 1 member A1 (UGT1A1) in hepatocytes (*17*) (*Fig. S1A*). Water soluble conjugated bilirubin is excreted via the bile or urine (*18*) (*Fig. S1A*).

Severe presentations of *P. falciparum* malaria are often associated with the accumulation of bilirubin in plasma, a condition referred to as jaundice of malaria, when associated with visible yellowing of the skin or white of the eyes (*1-3*). Jaundice in malaria develops once the rate of bilirubin production by BVRA exceeds that of bilirubin conjugation by UGT1A1 (*19*). Here we asked whether the accumulation of circulating bilirubin during *Plasmodium* spp. infection represents an adaptive or maladaptive metabolic response to malaria.

Results

Unconjugated Bilirubin limits *P. falciparum* malaria symptoms

A retrospective analysis of a cohort of patients with *P. falciparum* infection and asymptomatic or symptomatic malaria showed a positive correlation between the presence of clinical symptoms and parasite burden (*i.e.*, number of parasites *per* µL blood) (*Fig. 1A*), total circulating bilirubin (*Fig. 1B*), conjugated bilirubin (*Fig. 1C*) and unconjugated bilirubin (*Fig. 1D*). While these observations are consistent with previous studies (*1-3*), the standard analytical methods used in clinical practice do not accurately quantify unconjugated bilirubin in plasma (*16, 18, 20*). The binding of unconjugated bilirubin to albumin in plasma (*16*) interferes with the colorimetric reaction used in these assays (*16, 18, 20*). Moreover, byproducts of hemolysis, such as labile

heme, can interfere with these colorimetric assays, adding to their inaccuracy in the context of *Plasmodium* infection (*6, 11*).

To obtain a precise measure of unconjugated bilirubin in plasma we used a highly specific unconjugated bilirubin-inducible fluorescent protein (UnaG)-based assay (*Fig. S1B*) (*21, 22*). We found that the concentration of unconjugated bilirubin in plasma from asymptomatic *P. falciparum*-infected individuals ranged from 8–50 µM (*Fig. 1E*), that is, 3.75-fold higher than estimated using standard analytical methods (*Fig. S1C*). The concentration of unconjugated bilirubin in plasma from symptomatic *P. falciparum* malaria patients ranged from 14–67 µM (*Fig. 1E*), 2.67-fold higher than estimated using standard analytical methods (*Fig. S1C*) (*16, 18, 20*).

Using the same UnaG-based assay, we found that asymptomatic *P. falciparum* infection was associated with a higher ratio of circulating unconjugated over conjugated (*Fig. 1F*) or total (*Fig. S1D*) bilirubin as well as with a >10-fold higher ratio of circulating unconjugated bilirubin over parasite burden compared to symptomatic malaria (*Fig S1E*). As unconjugated bilirubin inhibits *P. falciparum* proliferation *in vitro* (*23*), we hypothesized that its accumulation in plasma represents an adaptive response to *P. falciparum* malaria.

Bilirubin is protective in experimental malaria

To test functionally the anti-malarial effect of unconjugated bilirubin, we infected C57BL/6J mice with *P. chabaudi chabaudi* AS (*Pcc*), a well-established non-lethal experimental model of malaria (*24*). Using the UnaG-based assay (*Fig. S1B*) (*21, 22*), we found that the concentration of circulating unconjugated bilirubin increased abruptly from day 4 to 7 post-infection to reach 13-31 µM (*Fig. 1G*), in the range of *P. falciparum* malaria patients (*Fig. 1E*). The specificity of

the UnaG-based assay was confirmed using *Blvra*-deficient (*Blvra*$^{-/-}$) mice (*22*), which did not express *Blvra* mRNA (*Fig. S2A*) and BVRA protein (*Fig. S2B,C*) and did not produce bilirubin (*Fig. 1G*).

Compared to the non-lethal outcome of *Pcc* infection in C57BL/6J *Blvra*$^{+/+}$ mice, all littermate C57BL/6J *Blvra*$^{-/-}$ mice succumbed to the infection within 7-10 days (*Fig. 1H*). This suggest that the production of bilirubin by BVRA confers protection against *Plasmodium* infection.

Using a biliverdin-inducible infrared fluorescent protein (iRFP)-based assay (*Fig. S2D*) (*22, 25*) to quantify the concentration of biliverdin in plasma, we found that the *Pcc*-infected *Blvra*$^{-/-}$ mice (*Fig. 1H*) accumulated relatively low levels of circulating biliverdin, in the range of 2.5-6 μM (*Fig. S2E*). This suggests that the lethal outcome of *Pcc* infection in *Blvra*$^{-/-}$ mice is not due to a putative accumulation of pathogenic levels of circulating biliverdin.

Administration of unconjugated bilirubin protected *Blvra*$^{-/-}$ mice from succumbing to *Pcc* infection (*Fig. 1I*). The protective effect of bilirubin was dose-dependent, that is, higher bilirubin dosage restored the survival of *Pcc*-infected *Blvra*$^{-/-}$ mice to the same extent as *Pcc*-infected *Blvra*$^{+/+}$ mice (*Fig. 1I*). This suggests that the lethal outcome of *Pcc* infection in *Blvra*$^{-/-}$ mice is attributable to a lack of bilirubin production.

We asked whether the production of bilirubin by BVRA is also protective against bacterial or viral infectious diseases. Disease severity and pathogen burden were indistinguishable in *Blvra*$^{-/-}$ and control *Blvra*$^{+/+}$ mice subjected to polybacterial sepsis induced by cecal ligation and puncture (*Fig. S3A-C*) or to influenza A virus infection (*Fig. S3D-F*). This suggests that the protective effect of unconjugated bilirubin is specific to hemolytic conditions, such as malaria.

UGT1A1 is deleterious in experimental malaria

The relative levels of *Hmox-1* mRNA expression were highly induced in different organs from *Pcc*-infected compared with non-infected C57BL/6J mice (*Fig. S4A*), consistent with previous findings (*14*). In contrast, the relative levels of *Blvra* mRNA expression were not induced in *Pcc*-infected compared with non-infected C57BL/6J mice (*Fig. S4B*). This suggests that the induction of bilirubin production in response to *Plasmodium* infection is dependent on the induction of HO-1 to increase the amount of biliverdin that can be reduced into bilirubin by BVRA (*Fig. S1A*).

Pcc infection was associated with a marked decrease in the relative level of hepatic *Ugt1a1* mRNA (*Fig. 1J, S4C*) and UGT1A1 protein (*Fig. 1J, S4D*) expression, 7 days post-infection, compared to non-infected controls. This suggests that the accumulation of circulating bilirubin in response to *Plasmodium* infection is sustained by the repression of hepatic UGT1A1 (*Fig. S1A*).

To test whether inhibition of hepatic bilirubin conjugation is protective against malaria we used *Pcc* infection in DBA/2 mice, as a lethal experimental model of malaria (*26*). Hepatic UGT1A1 was repressed specifically in the liver of newborn DBA/2 mice, transduced with a recombinant adeno-associated virus serotype 8 (AAV8) encoding the *Staphylococcus aureus* (Sa) CRISPR associated protein 9 (Cas9) and a single guide RNA (gRNA) targeting *Ugt1a1* (AAV8-gRNA-*Ugt1a1*), as previously described (*27*). Adult DBA/2 mice transduced with AAV8-gRNA-*Ugt1a1* presented lower levels of hepatic UGT1A1 protein, compared to controls transduced with a AAV8 encoding SaCas9 without the targeting gRNA (AAV8-Cas9) (*Fig. S4E,F*). This was associated with an increase in the concentration of unconjugated bilirubin in plasma (*Fig. 1K*) and with a major survival advantage against *Pcc* infection, compared to control *Pcc*-infected DBA/2 mice transduced with AAV8-Cas9 (*Fig. 1L*). These observations suggested

that the repression of hepatic UGT1A1 in response to *Plasmodium* infection is protective against malaria.

Bilirubin reduces *Plasmodium* burden

P. falciparum proliferation is inhibited by unconjugated bilirubin *in vitro* (*23*), suggesting that the accumulation of unconjugated bilirubin in plasma confers resistance to malaria (*i.e.,* reduces the host parasite burden). In strong support of this hypothesis, *Pcc*-infected *Blvra*$^{-/-}$ mice presented a clear increase in the percentage of circulating infected-RBC (iRBC; parasitemia) 7-9 days post-infection (*Fig. 2A*), accounting for 10-fold increase in the number of iRBC (*i.e.,* parasite burden), compared to *Pcc*-infected *Blvra*$^{+/+}$ mice (*Fig. 2B*). Consistent with this observation, the administration of unconjugated bilirubin to *Pcc*-infected *Blvra*$^{-/-}$ mice reduced parasitemia (*Fig. S5A*) and parasite burden, compared to vehicle-treated *Pcc*-infected *Blvra*$^{-/-}$ mice (*Fig. S5B*). Moreover, repression of bilirubin conjugation also reduced the parasitemia (*Fig. S5C*) and parasite burden (*Fig. S5D*) of *Pcc*-infected DBA/2 mice transduced with a AAV8-gRNA-*Ugt1a1* compared with controls transduced with a AAV8-Cas9. These observations suggest that the accumulation of unconjugated bilirubin in plasma confers resistance to *Plasmodium* infection.

Bilirubin targets *Plasmodium* inside RBC

As unconjugated bilirubin diffuses across cellular membranes (*28, 29*), we tested whether unconjugated bilirubin targets *Plasmodium* inside the RBC. We performed single-cell RNA sequencing (scRNAseq) of circulating *Pcc*-infected RBC (iRBC) FACS-sorted from *Blvra*$^{-/-}$ *vs.* *Blvra*$^{+/+}$ mice. Single parasite transcriptomes were assigned to specific developmental stages,

based on a single-cell malaria atlas (*30*). Visualization, using uniform manifold approximation and projection (UMAP), revealed a circular orientation of parasites throughout the asexual cycle: Rings (clusters 1, 2), Trophozoites (clusters 3, 4), Schizonts (clusters 5, 6) and developing Gametocytes (cluster 7) (*Fig. S6A,B; Data table S1*), consistent with previous descriptions (*30-32*).

Circulating iRBC from *Blvra*$^{-/-}$ mice exhibited a marked increase in the proportion (*Fig. 2C,D*) and relative number (*Fig. 2E*) of parasite transcriptomes corresponding to metabolically-active early trophozoites (cluster 3). This was associated with loss of early (cluster 5) and late (cluster 6) schizonts as well as early rings (cluster 1), and with a decrease in late rings (cluster 2) and late trophozoites (cluster 4) (*Fig. 2C,D*), as confirmed by morphological analyzes (*Fig. S7A-C*). These changes were not attributed to modulation of parasite sequestration in different organs, as determined by shifting the "light cycle" of infection (*Fig. S7D*).

Progression of *Pcc* infection in *Blvra*$^{+/+}$ mice was associated with the expected parasite developmental trajectory whereby late trophozoites (cluster 4) developed into early (cluster 5) and late (cluster 6) schizonts to give rise to early (cluster 1) ring stages, as assessed by RNA velocity analyses (*33*) (*Fig. 2F*). Progression through late rings (cluster 2) and early trophozoites (cluster 3) was diffuse in *Blvra*$^{+/+}$ mice and contrasted sharply with the progression of the same parasite developmental stages in *Blvra*$^{-/-}$ mice (*Fig. 2F*). This suggests that bilirubin reduces the fitness of early trophozoites from *Blvra*$^{+/+}$ compared with *Blvra*$^{-/-}$ mice.

Late ring stages (cluster 2) from *Blvra*$^{-/-}$ mice showed a marked increase in gene expression profiles associated with peptidase activity, heme binding, electron transport chain, proteosome activity and catabolic processes, compared to ring stages from control *Blvra*$^{+/+}$ mice (*Fig. S8, S9A; Data tables S2,3*). Early trophozoites (cluster 3) in *Blvra*$^{-/-}$ mice also showed a clear increase in gene expression associated with peptidase activity, ATP-dependent protein folding

chaperone and unfolded protein binding, proteosome core complex, ubiquitin and catabolic processes, compared with early trophozoites from control *Blvra*$^{+/+}$ mice (*Fig. S8, S9B; Data tables S2,3*). In addition, there was a concomitant decrease in gene expression profiles associated with chromatin structure (*Fig. S8, S9B; Data tables S2,3*). Late trophozoites (cluster 4) in *Blvra*$^{-/-}$ mice showed an increase in gene expression profiles associated with ATP-dependent protein folding, RNA binding and translational activity, glycolytic, pyruvate and carbohydrate, ADP, and ATP metabolic processes (*Fig. S8, S9C; Data tables S2,3*). Moreover, there was a concomitant decrease in gene expression profiles associated with structural constituents of chromatin, DNA replication and chromosome organization/segregation (*Fig. S8, S9C; Data tables S2,3*).

Bilirubin reduces parasite virulence

Among the 1019 differentially expressed genes in *Pcc* late rings and early and late trophozoites from *Blvra*$^{-/-}$ compared with *Blvra*$^{+/+}$ mice (*Fig. S8*), 118 (11.6%) (*Data tables S2,4*) were previously linked to *Pcc* virulence (*34*). These included 53 upregulated and 65 downregulated genes in *Blvra*$^{-/-}$ compared with *Blvra*$^{+/+}$ mice (*Data tables S2,4*). The direction of gene regulation showed a significant association with previous studies (Fisher's exact test, $p<0.0001$, *Data tables S2,4*) for 92% of the upregulated genes (49 out of 53) and 49% of downregulated genes (32 out of 65) (*34*). Among the upregulated genes were four *Plasmodium* Interspersed Repeat (*pir*) genes (*PCHAS_030190, PCHAS_041960, PCHAS_104230*, and *PCHAS_110030*), encoding variant surface CIR proteins linked to parasite "immune evasion" (*35, 36*) and genes involved in the parasite metabolic adaptation (*34*). Other virulence genes, included 17 *Pc-fam* (or rodent malaria parasites; RMP-fam) genes (*37*); and eight genes encoding exported proteins (*34*),

including the *cir* gene *PCHAS_110030*, a *P. falciparum* RIF orthologue linked to *Pcc* virulence (*36, 38*). These observations suggest that *Pcc* parasite virulence (*i.e.,* ability to cause disease or damage to the host) increases in *Blvra*$^{-/-}$ compared with *Blvra*$^{+/+}$ mice.

We then asked whether the genetic fingerprint of higher virulence in parasites from *Blvra*$^{-/-}$ compared with *Blvra*$^{+/+}$ mice contributes to increased malaria mortality. In strong support of this hypothesis, the incidence of mortality (*Fig. 2G*), parasitemia and parasite burden (*Fig. 2H*) were increased in *Blvra*$^{-/-}$ mice infected with parasites isolated from *Blvra*$^{-/-}$ compared with *Blvra*$^{+/+}$ mice (*Fig. 2G,H*). This suggests that the protective effect of bilirubin against malaria is mediated via a resistance mechanism that reduces *Plasmodium* burden and virulence.

Bilirubin accumulates in *P. falciparum*-infected RBC

To explore the mechanism via which bilirubin reduces *Plasmodium* virulence, we asked whether bilirubin targets *P. falciparum* directly inside RBC *in vitro*. We used scanning electron microscopy (SEM) to confirm that unconjugated bilirubin precipitates in culture medium (*39*) (*Fig. S10A*), accounting for a 67% reduction of its expected concentration (*Fig. S10B-D*), as determined using the UnaG-based assay (*Fig. S1B,C*) (*21, 22*). There was a marked accumulation of bilirubin in *P. falciparum* 3D7 iRBC exposed *in vitro* to unconjugated bilirubin, at a concentration in the range of *P. falciparum* seen in malaria patients (*Fig. 3A, Data table S5*). By contrast, there was no detectable accumulation of bilirubin in non-infected RBC, similar to vehicle-treated controls (*Fig. 3A, Data table S5*). This suggests that unconjugated bilirubin accumulates specifically in *Plasmodium*-iRBC when present at a concentration in the range of that seen in *P. falciparum* malaria patients.

Bilirubin arrests and kills *P. falciparum*

Unconjugated bilirubin inhibited the proliferation of *P. falciparum* 3D7 (*Fig. 3B*), as well as that of the *P. falciparum* multidrug-resistant Dd2 (*Fig. S11A*) and IPC 5202 (*Fig. S11B*) strains *in vitro*. This anti-proliferative effect was dose-dependent, that is, the higher the concentration of bilirubin the lower *P. falciparum* proliferation (*Fig. 3B; Fig. S11A,B*). Importantly, the anti-proliferative effect of bilirubin occurred *in vitro*, at concentrations in the range of those seen in *P. falciparum* malaria patients, as assessed using the UnaG-based assay (*Fig. 1E*).

The anti-proliferative effect of bilirubin was not associated with the induction of hemolysis, as assessed by microscopy (*Fig. 3B; Fig. S11A,B*) and confirmed by lactate dehydrogenase (LDH) release from lysing RBC (*Fig. S11C*). This suggests that unconjugated bilirubin targets *Plasmodium* specifically in RBC without causing hemolysis.

A water-soluble bilirubin ditaurate derivative failed to inhibit the proliferation of *P. falciparum* 3D7 (*Fig. S11D*), instead promoting ring stage proliferation at concentrations in the 40-80 µM range (*Fig. S11D*). This suggests that the anti-proliferative effect of bilirubin is restricted to its unconjugated form, which diffuses across cellular membranes (*28, 29*) and accumulates specifically in *Plasmodium*-iRBC (*Fig. 3A, Data table S5*).

Biliverdin had no anti-proliferative effect on *P. falciparum* 3D7 (*Fig. S12A*), Dd2 (*Fig. S12B*) or IPC 5202 (*Fig. S12C*) strains, at concentrations up to 10-fold greater than those detected in *Pcc*-infected *Blvra*$^{-/-}$ mice (*Fig. S2D*). Of note, at a maximal concentration of 120µM there was a marginal effect of biliverdin on the proliferation of *P. falciparum* 3D7 (*Fig. S12A*) and IPC 5202 (*Fig. S12C*) strains, consistent with previous observations (*40*). This suggests that circulating biliverdin does not exert anti-proliferative effects on blood stages of *Plasmodium* at concentrations in the range of those detected in *Pcc*-infected *Blvra*$^{-/-}$ mice (*Fig. S2E*).

Bilirubin impairs *Plasmodium* energy metabolism

Unconjugated bilirubin caused a striking accumulation of glucose and, to a lower extent, glucose-6-phosphate in *P. falciparum* 3D7 iRBC, compared to control iRBC exposed to vehicle (*Fig. 3C, Data table S5*). Moreover, unconjugated bilirubin reduced the relative levels of succinate, aspartate, fumarate and adenosine monophosphate (AMP) in *P. falciparum* 3D7 iRBC, compared to control vehicle-treated iRBC (*Fig. 3C, Data table S5*). This suggests that bilirubin compromises *P. falciparum* central carbon metabolism (*41*). Consistent with this notion, *Pcc* ring stages and trophozoites from *Blvra*$^{-/-}$ mice showed an increase in the expression of a number of glycolytic genes, including *PCHAS-121500* (enolase, putative; ENO); *PCHAS-100970* (glucose-6-phosphate isomerase, putative), *PCHAS-1329700* (phosphoglycerate kinase, putative), *PCHAS-082370* (phosphoglycerate kinase; PGK, putative) and *PCHAS-091620* (phosphoglycerate mutase; PGM1, putative), compared to control *Blvra*$^{+/+}$ mice (*Fig. 3D, Data tables S2,3*). This suggests that unconjugated bilirubin compromises the central carbon metabolism of *Plasmodium* via a mechanism that targets the expression of the parasite´s glycolytic genes.

Moreover, *Pcc* ring stages and early trophozoites from *Blvra*$^{-/-}$ mice also presented an increase in the expression of several genes involved in mitochondrion ATP metabolic processes, including *PCHAS-041070* (ATP synthase F0 subunit d-like protein, putative), *PCHAS-145260* (ATP synthase subunit beta, mitochondrial, putative), *PCHAS-031590* (ATP synthase subunit alpha, mitochondrial, putative) and *PCHAS-MIT0001* (cytochrome c oxidase subunit 3; COX3) (*Fig. 3D, Data tables S2,3*). This suggests that unconjugated bilirubin compromises *Plasmodium* mitochondrion function *in vivo*.

Bilirubin disrupts *Plasmodium* mitochondrion function

Consistent with the notion that unconjugated bilirubin compromises *Plasmodium* spp. mitochondrion, *P. falciparum* 3D7 mitochondrion volume was severely reduced upon *in vitro* exposure to unconjugated bilirubin, as assessed by flow cytometry (*Fig. 3E*) and confirmed by live confocal microscopy imaging (*Fig. S13A,B*). This effect was dose-dependent, that is, the higher the concentration of bilirubin, the lower the parasite's mitochondrion volume (*Fig. 3E*), at concentrations in the range of *P. falciparum* malaria patients, as assessed using the UnaG-based assay (*Fig. 1E*). Equimolar concentrations of biliverdin failed to reduce *P. falciparum* mitochondrion volume *in vitro* (*Fig. S13C*).

Unconjugated bilirubin decreased *P. falciparum* 3D7 mitochondrion membrane potential (*Fig. S14A*) and superoxide accumulation (*Fig. S14B*) *in vitro*, compared to vehicle-treated controls (*Fig. S14A,B*). This effect was dose-dependent, that is, the higher the concentration of bilirubin, the lower the parasite's membrane potential (*Fig. S14A*) and superoxide accumulation (*Fig. S14B*). Equimolar amounts of biliverdin failed to reduce *P. falciparum* 3D7 mitochondrion membrane potential (*Fig. S14C*) or superoxide accumulation (*Fig. S14D*).

Bilirubin represses *Plasmodium´s* mitochondrion pyrimidine synthesis

Plasmodium spp. replication relies on *de novo* pyrimidine synthesis via the conversion of dihydroorotate (DHO) into orotate, catalyzed by the mitochondrial inner membrane dihydroorotate dehydrogenase (DHODH) (*42*). Exposure of *P. falciparum* 3D7 iRBC to unconjugated bilirubin caused a marked reduction in DHO, orotate and uridine monophosphate (UMP), a downstream product of DHODH in the parasite´s *de novo* pyrimidine synthesis (*Fig.*

3F, Data table S5). This suggests that the anti-proliferative effect of unconjugated bilirubin is exerted via a mechanism that impairs mitochondrion-dependent pyrimidine synthesis.

Bilirubin acts beyond *Plasmodium´s* mitochondrion

To determine whether the anti-proliferative effect of bilirubin relies exclusively on the inhibition of mitochondrion pyrimidine synthesis, we used a transgenic *P. falciparum* D10 strain expressing a cytoplasmic *Saccharomyces cerevisiae* DHODH (*Pf*D10^{TgDHODH}) (*42*). In contrast to the parental *Pf*D10 strain, *Pf*D10^{TgDHODH} parasites can support pyrimidine synthesis irrespectively of the mitochondrion (*42*). As expected (*43*), inhibition of the mitochondrion electron transport chain cytochrome bc_1 complex by Atovaquone (ATQ) arrested the proliferation and killed the parental *Pf*D10 but not the *Pf*D10^{TgDHODH} strain (*Fig. S15A*). In contrast however, unconjugated bilirubin arrested the proliferation and killed both the parental *Pf*D10 and the *Pf*D10^{TgDHODH} strains (*Fig. 3G; Fig. S15B*). This suggests that the anti-proliferative effect of bilirubin acts beyond the inhibition of *P. falciparum* pyrimidine synthesis.

Bilirubin inhibits Hz crystallization

Exposure of *P. falciparum* 3D7 to unconjugated bilirubin *in vitro* was associated with dispersion of hemozoin (Hz) crystals in the iRBC, as visualized and quantified by live confocal microscopy imaging (*Fig. 4A; Fig. S16A,B*). Equimolar amounts of biliverdin had no effect on Hz, similar to vehicle controls (*Fig. S16A-C*). This suggests that bilirubin interferes directly or indirectly with the detoxification of the heme extracted from hemoglobin into Hz crystals.

We then asked whether bilirubin interferes directly with Hz crystallization. Consistent with this hypothesis, computational simulation of a putative bilirubin docking in the deep groove on

the fastest growing (*i.e.,* 001) face of the crystal suggested that bilirubin interferes directly with Hz crystallization (*Fig. S17*). The two top scoring docking poses suggest that the adsorption of bilirubin to the crystal surface is facilitated by hydrogen bonding between its carboxylic acid moiety and the pyrrole groups of heme in the nascent Hz crystals (*Fig. S17*). This suggested that bilirubin hinders heme incorporation in nascent Hz crystals, impairing the parasite´s capacity to neutralize cytotoxic labile heme (*44, 45*). This hypothesis was confirmed using a standard *in vitro* assay to quantify the crystallization of β-hematin, a synthetic heme adduct chemically and spectroscopically identical to Hz (*46*). Unconjugated bilirubin inhibited β-hematin formation (*Fig. 4B*), mediated by the lipid mimic Nonidet P-40 detergent, as monitored by the accumulation of heme as a *bis*-pyridyl complex (*47*). The IC_{50} of bilirubin was 1-1.2 mM, that is, 50-60 times less potent than that of chloroquine (IC_{50}=20μM) in the same assay.

Consistent with the notion that bilirubin inhibits Hz crystallization *in vitro, Pcc* infection in *Blvra*$^{-/-}$ mice was associated with higher levels of Hz accumulation in circulating iRBC, as compared to iRBC from control *Blvra*$^{+/+}$ mice, at the light and dark cycle of *Pcc* infection (*Fig. 4C*). This suggests that bilirubin exerts an anti-malarial effect via Hz crystallization, akin to quinoline-based antimalarial drugs (*45, 48*).

Bilirubin disrupts *P. falciparum* food vacuole

Inhibition of Hz crystallization by quinoline-based antimalarial drugs compromises the parasite´s digestive food vacuole (*45, 48*), suggesting that bilirubin also disrupts the parasite's food vacuole. In support of this hypothesis, unconjugated bilirubin disrupted the food vacuole of *P. falciparum* 3D7 trophozoites, as revealed by leakage of its acidic content, quantified by confocal

microscopy live imaging (*Fig. 4D; Fig. S18A,B*). Equimolar amounts of biliverdin failed to disrupt *P. falciparum* food vacuole, similar to vehicle-treated controls (*Fig. S18A-C*).

Disruption of *P. falciparum* food vacuole by bilirubin was further confirmed by transmission electron microscopy (TEM) (*Fig. 4E; Fig. S19*), revealing the formation of multilamellar bodies (*Fig. 4E; Fig. S19*), reminiscent to those observed when targeting endosomal vesicle delivery to the food vacuole (*49*). This was associated with the accumulation of Hz crystals in the parasite's cytoplasm (*Fig. 4E; Fig. S19*), with a structural appearance consistent with the loss of its characteristic sharp rectangular morphology (*Fig. 4E; Fig. S19*). These "rounded-edged" cytoplasmic Hz crystals were not observed in parasites exposed to equimolar amounts of biliverdin or to vehicle (*Fig. 4E; Fig. S19*).

The *Plasmodium* food vacuole is vital for the acquisition of essential amino acids (AA) contained in hemoglobin (*50*). That bilirubin impairs this vital process is supported by the reduction in the relative amount of these essential AA in *P. falciparum* 3D7 trophozoites exposed to unconjugated bilirubin, as illustrated for: Leucine (Leu), Phenylalanine (Phe), Valine (Val), Threonine (Thr), Tryptophan (Trp), Lysine (Lys) and Proline (Pro) (*Fig. 4F, Data table S5*). This was also observed for non-essential AA contained in hemoglobin, including: Aspartate (Asp) (*Fig. 3C, Data table S5*), Arginine (Arg), Tyrosine (Tyr) and Serine (Ser) (*Fig. S20A, Data table S5*). In sharp contrast, AA not contained in hemoglobin, which are not acquired via the food vacuole (*50*), were not affected by unconjugated bilirubin, as illustrated for methionine (Met) and isoleucine (Ile) (*Fig. 4F*). Moreover, bilirubin had no effect on the AA content of non-infected RBC, compared to vehicle-treated control*s* (*Fig. S20B, Data table S5*). This suggests that bilirubin compromises specifically the capacity of *P. falciparum* food vacuole to extract essential AA from hemoglobin.

Several genes involved in hemoglobin digestion by the food vacuole were also increased in *Pcc* ring stages and trophozoites from *Blvra*$^{-/-}$ compared with *Blvra*$^{+/+}$ mice (*Fig. S20C, Data tables S2,3*). These included *PCHAS-083340* (M18 aspartyl aminopeptidase, putative), *PCHAS-113650* (falcilysin; FLN, putative; highly active at acidic pH consistent with its critical role in hemoglobin degradation), *PCHAS-131350* (M17 leucyl aminopeptidase, putative) and *PCHAS-131310* (M17 leucyl aminopeptidase, putative) (*Fig. S20C, Data tables S2,3*), suggesting that bilirubin also acts *in vivo* to compromise the capacity of *Plasmodium* trophozoites to extract essential AA from hemoglobin, likely contributing to the anti-malarial effects of unconjugated bilirubin.

Discussion

Our findings support the notion that the accumulation of unconjugated bilirubin in plasma during *Plasmodium* spp. infection (*Fig. 1B-E,G*) represents a protective metabolic response to malaria (*Fig. 1H,I,L*). This is in keeping with the growing evidence suggesting that bilirubin exerts major physiological functions (*22, 51, 52*), challenging the strongly held notion that unconjugated bilirubin is a final "waste product" that accumulates in plasma due to liver dysfunction (*53*).

The protective effect of unconjugated bilirubin against *Plasmodium* infection is propelled by BVRA (*Fig. 1G,H*) and sustained by the inhibition of bilirubin conjugation via the repression of hepatic UGT1A1 (*Fig. 1J-L*). Consistent with our findings, several *UGT1A1* genetic hypomorphic variants are associated with mild unconjugated nonhemolytic hyperbilirubinemia in individuals of African ancestry, with the longest co-evolution with *Plasmodium* (*54, 55*). These include the hypomorphic variant *UGT1A1**28 (rs3064744) responsible for Gilbert's syndrome (*19, 56*), which reduces *UGT1A1* transcription by 70% in an estimated prevalence of 15-25% of individuals of African ancestry, compared to 0-5% and 5-10% in Asian and

Caucasian ancestries (*54*). However, an association between polymorphisms in or near the *UGT1A1* locus (chr2:233,760,270-233,773,300) and *P. falciparum* malaria severity was not reported in previous GWAS studies (*57-61*). One possible explanation for this is that *UGT1A1* genetic variants can increase the incidence and severity of neonatal jaundice (*54, 55*). Moreover, *UGT1A1* genetic variants might co-segregate with balanced polymorphisms conferring protection against malaria via the induction of heme catabolism, such as sickle hemoglobin (*10*).

Targeting of *Plasmodium* inside RBC by unconjugated bilirubin (*Fig. 3A*) is consistent with unconjugated bilirubin crossing cellular membranes (*28, 29*), despite its binding to albumin in plasma (*16*). Presumably this occurs via aqueous diffusion (*62*), suggesting that cellular membranes have higher affinities for unconjugated bilirubin than albumin (*62*).

The inhibition of *Plasmodium* spp. proliferation (*Fig. 2A, 3B, S5*) and virulence (*Fig. 2G, Data tables S2,4*) by unconjugated bilirubin is associated with repression of the parasite´s capacity to consume glucose via glycolysis (*Fig. 3C,D*), presumably inhibiting mitochondrion tricarboxylic acid (TCA) cycle function (*Fig. 3C,D*). Moreover, unconjugated bilirubin disrupts the parasite´s mitochondrion structure (*Fig. 3E, S13A,B*) and function (*Fig. S14A*), compromising *de novo* pyrimidine synthesis (*Fig. 3F*) and therefore inhibiting *Plasmodium* spp. proliferation (*42*). This, however, is not sufficient to fully explain the anti-malarial effects of bilirubin (*Fig. 3G*).

While *Plasmodium* spp. evolved to detoxify redox-active labile heme into redox-inert Hz crystals, the proliferation of these parasites inside RBC is associated with intravascular hemolysis and the release of labile heme into plasma (*6, 8-11*). This induces the expression of HO-1 in the infected host, which catabolizes labile heme into biliverdin (*8, 9, 14*), fueling the production of bilirubin by BVRA. As it accumulates in plasma, unconjugated bilirubin inhibits Hz crystallization (*Fig. 4A-C, S16A, B*), similar to, although far less potent than quinoline-based

antimalarial drugs such as chloroquine (*Fig. 4B*) (*45, 48*). The inhibition of Hz crystallization leads to the disruption of the parasite´s food vacuole (*Fig. 4D,E, S18*), compromising the extraction of essential AA from hemoglobin (*Fig. 4F*) while presumably leading to accumulation of cytotoxic labile heme.

In conclusion, the induction of bilirubin production in response to *Plasmodium* spp. infection is a metabolite-based resistance mechanism (*63*) against malaria. We speculate that while evolutionarily conserved, this defense strategy carries as an evolutionarily trade-off (*64*), the insidious prevalence of neonatal jaundice (*65, 66*), which can lead to encephalopathy (*67*). Considering the selective pressure exerted by malaria over the course of human evolution (*68*), it is conceivable that the anti-malarial effects of unconjugated bilirubin outcompeted the fitness costs associated with high incidence of neonatal jaundice in populations originating in endemic areas of malaria (*69, 70*).

Limitations

The association of asymptomatic *P. falciparum* malaria with a higher ratio of unconjugated over conjugated bilirubin, compared to symptomatic *P. falciparum* malaria, suggests that unconjugated bilirubin counters the transition of asymptomatic towards symptomatic *P. falciparum* malaria. While consistent with the observation that repression of bilirubin conjugation is protective against malaria in mice, whether this is also the case for *P. falciparum* malaria remains to be established. Moreover, given the limited number of *P. falciparum* malaria patients analyzed these observations should be confirmed by future independent studies.

The observation that *Plasmodium* infection associated with the repression of bilirubin conjugation in mice, suggest that the accumulation of unconjugated bilirubin in plasma from

asymptomatic *P. falciparum* malaria patients is protective against the onset of disease. This, however, is a hypothesis that remains to be established. If this was to be the case one would expect future GWAS studies to identify genetic polymorphisms regulating bilirubin conjugation to be associated with *P. falciparum* malaria incidence and/or outcome.

The molecular mechanism via which bilirubin represses *P. falciparum* proliferation was associated with disruption of the parasite´s mitochondrion and food vacuole but whether these are functionally linked is not clear.

While our findings suggest that the anti-malarial effect of bilirubin is exerted via a direct effect on the parasite, this should not exclude bilirubin from exerting additional protective effects that would act irrespectively of the parasite. These are likely to be exerted via its anti-oxidant effects, which should contribute to limit tissue damage and possibly enforce disease tolerance to malaria.

Materials and Methods

Human data

Clinical patients' data were collected from a prospective clinical cohort study, conducted between March and July 2022 at Centre de Recherches Médicales de Lambaréné (CERMEL), Gabon. The study was approved by the ethics committee of CERMEL (DEMIT-GAB: CEI 18/2021, and all patients provided written informed consent and were included in this analysis if they fulfilled the following criteria: a) age ≥18 years; b) microscopically confirmed asexual *P. falciparum* infection by positive blood smear; c) blood drawn before or ≤24h after initiation of antimalarial treatment. Patients were excluded in case of known liver (e.g., hepatitis, hepatic cancer) or hematologic disease, pregnancy or breastfeeding, mixed *Plasmodium* infection and

with missing initial parasitemia data, hematology data, liver function data or bilirubin data. Patients were grouped as asymptomatic within 7 days before and 7 days after diagnosis or symptomatic malaria according to WHO criteria (*71*). Among 42 participants meeting the criteria for this analysis, the mean age was 33.1 (SD=16.97) years (asymptomatic: 36.0 (SD=19.6); symptomatic: 29.9 years (SD=13.2). Overall, 48% (20/42) were male and 52% (22/42) female (males among asymptomatic: 45% (10/22); symptomatic: 50% (10/20)). Median initial parasitemia was 576 iRBC (IQR: 131 to 4,201) *per* µL (asymptomatic: 322,5 [110 to 851]; symptomatic: 4,289 [322 to 48,218]). Unconjugated bilirubin was measured exclusively by the UnaG-based assay (*21, 22*) in 4 asymptomatic and 1 symptomatic malaria patients out of the 42 patients. Parasitological analyses, hematology and biochemistry were performed by accredited laboratories at CERMEL and Charité - Universitätsmedizin Berlin. Study data were collected and managed using REDCap (Research Electronic Data Capture) tools hosted at CERMEL and Charité - Universitätsmedizin Berlin (*72*).

Mice

Mice were bred and maintained under specific pathogen-free (SPF) conditions at the Gulbenkian Institute of Molecular Medicine (GIMM), housed at standard *vivarium* temperature (22ºC) on a regular light cycle, lights on from 8:00 am (ZT 0) to 8:00 pm (ZT 12). When indicated, mice were kept on inverted light cycle, lights on from 8:00 pm (ZT 0) to 8:00 am (ZT 12). Mice were maintained with free access to water and standard chow pellets (*ad libitum*). All experimental protocols were approved in a two-step procedure, by the Animal Welfare Body of the GIMM and by the Portuguese National Entity that regulates the use of laboratory animals in research (Direção Geral de Alimentação e Veterinária; DGAV). Experimental procedures followed the Portuguese (Decreto-Lei nº 113/2013) and European (Directive 2010/63/EU) legislation.

C57BL/6J and DBA/2 mice were obtained from the GIMM animal facility. C57BL/6J *Blvra*$^{-/-}$ mice were generated at Ozgene (Australia), as described (*22*). Age-matched wild-type C57BL/6J mice were used as controls and co-housed at least two weeks with *Blvra*$^{-/-}$ *mice* before infection.

Plasmodium chabaudi chabaudi AS infection and disease assessment

Mice (females and males, 8-14 weeks old) were infected with *Plasmodium chabaudi chabaudi* AS (*Pcc* AS) or transgenic GFP-expressing *Pcc* AS (*Pcc* AS-GFP$_{ML}$) (*73*). Infections were performed by intraperitoneal (*i.p.*) administration of freshly isolated blood (Passage 34-39; $2x10^6$ or $2x10^5$ infected RBC diluted in 200 µL PBS) collected from a previously infected C57BL/6J mouse. Mice were monitored daily from day 0 (day of infection) onwards for parasitemia (% infected RBC; iRBC), parasite burden (number of iRBC *per* µL of blood) and survival, essentially as described (*14, 31*). Briefly, the number of RBC *per* µL of blood was quantified by flow cytometry (LSR Fortessa X20 analyzer; BD Bioscience) using a standard concentration of reference latex beads (10 µm; Coulter® CC Size Standard L10, Beckman Coulter, # 6602796), gating on RBC, based on size and granularity and on bead population. For *Pcc* AS, parasitemia was determined manually by optical microscopy, counting the number of iRBC in at least 4 fields of Giemsa-stained blood smears (1000x magnification). For *Pcc* AS-GFP$_{ML}$, parasitemia was determined by flow cytometry, according to the percentage of RBC expressing GFP (GFP^+ RBC). Parasite burden, expressed as iRBC/µL, was determined by multiplying the parasitemia by the number of RBC. Representative Giemsa-stained thin blood smear images were acquired suing a Zeiss Imager Z2/ApoTome.2, equipped with an Axiocam 105 color camera, using the 100x 1. 4NA Oil immersion objective, in a 5×5 tile stitched with Zeiss's ZEN v3.1. The images were analyzed using the Fiji Software (ImageJ) and the background in parasite RGB images was

corrected using the Color Correct plugin for Fiji, contributed by Gabriel Landini (https://github.com/landinig/IJ-Colour_Correct/blob/main/colour_correct.zip).

Bilirubin supplementation during Plasmodium infection

Blvra$^{-/-}$ mice were infected with *Pcc* AS-GFPML (2x10^5 iRBC, 200µL, *i.p.*) and monitored as described above. Bilirubin (Frontier Scientific) stock solutions were prepared as described (*74*). Briefly, bilirubin was dissolved in 0.2N NaOH, buffered to pH 7.4 using 0.2N HCl, filtered (70µm cell strainer) to remove precipitates and stored (-80ºC). Absorbance was determined using a spectrophotometer (SmartSpec 3000) at 460nm. The concentration was calculated considering 53,846 cm^{-1} M-1^{-1} as molar extinction coefficient and following the Lambert-Beer law (A460nm=ε.C. l). Bilirubin was administered *i.p.* at 30mg/Kg or 3mg/Kg, , once daily, from day 4 to day 15 after infection.

Repression of hepatic Ugt1a1 in vivo

A recombinant adeno-associated virus serotype 8 (AAV8) encoding the *Staphylococcus aureus* (Sa) CRISPR associated protein 9 (Cas9) and a single guide RNA (gRNA) targeting *Ugt1a1* (AAV8-gRNA- *Ugt1a1*) was administered to 2-4 days old DBA/2 mice (3x10^{14} viral particles/Kg body weight, in PBS; *i.v.* retro-orbitally), as described (*27*). Controls were transduced with a AAV8 encoding SaCas9 without the targeting gRNA (AAV8-Cas9). Female transduced mice were infected with *Pcc* (2x10^6 iRBC, 200µL, *i.p.*) at ~10 weeks after birth and monitored for survival, parasite burden and disease severity, as described above. Adult male transduced mice were sacrificed for organ collection to assess *Ugt1a1* deletion efficiency by Western blot.

Plasmodium virulence assay

Pcc parasites were adoptively transferred from *Blvra*$^{+/+}$ *vs. Blvra*$^{-/-}$ mice into female *Blvra*$^{-/-}$ mice, essentially as described (*31*). Briefly, blood was collected from both *Blvra*$^{+/+}$ and *Blvra*$^{-/-}$ mice 7 days after *Pcc* infection and the same number of iRBC ($2x10^6$; 200 µL PBS) were passively transferred (*i.p.*) into recipient *Blvra*$^{-/-}$ mice, monitored daily for disease assessment and survival, as described above.

Pcc-infected RBC sequestration

Blvra$^{+/+}$ and *Blvra*$^{-/-}$ mice were infected with *Pcc* and kept on inverted light cycle, lights on from 8:00 pm (ZT 0) to 8:00 am (ZT 12). Mice were sacrificed (CO_2 asphyxiation) 7 days after infection, perfused *in toto* via transcardiac infusion of ice-cold PBS (1X, 15 mL), organs were harvested, snap frozen in liquid nitrogen and stored at -80°C. The accumulation of *Pcc* AS 18S rRNA in different organs was quantified by qRT-PCR. RNA extraction and qRT-PCR were performed as described in the section RNA extraction and qRT-PCR.

Cecal Ligation and Puncture (Sepsis)

Cecal Ligation and Puncture (CLP) was performed in *Blvra*$^{+/+}$ and *Blvra*$^{-/-}$ mice (females and males, 8-14 weeks old), essentially as described (*75*). Briefly, mice were anesthetized (Ketamine: 12 mg/mL; and Xylazine: 1.6 mg/mL in 1xPBS; 180-200 µL *i.p.*) and subjected to a 15-20% cecum ligation and double puncture with a 23 Gauge (G) needle. A small amount of feces was extruded, and the cecum was carefully placed back into the abdominal cavity. All animals received 0.9% saline (40 mL/Kg, *i.p.*) and Imipenem/Cilastatin (25 mg/Kg, *i.p.*), starting 2h after CLP and every 12h for 3 days. Mice were monitored daily from day 0 (day of infection) onward for body weight (Ohaus® CS200 scaler, Sigma Aldrich), rectal temperature (Rodent

thermometer; BIO-TK8851, Bioset), blood glucose concentration (Accu-CHECK Performa glucometer, Roche), and survival.

Bacterial load

Mice were sacrificed 24 hours after CLP and peritoneal fluid was obtained by peritoneal lavage (7 mL sterile PBS). Mice were perfused with sterile ice cold 1x PBS. Whole organs were harvested and homogenized under sterile conditions in 1 mL sterile ice cold 1x PBS using a dounce tissue grinder (Sigma Ref: D8939-1SET). Serial dilutions were plated onto TrypticaseSoy Agar II with 5% Sheep Blood plates (Becton Dickinson Ref:254053) and incubated (24 h at 37 °C) in air 5% CO_2 (aerobes) or in an airtight container equipped with the GasPak anaerobe container system (Becton Dickinson Ref 260678). Anaerobic conditions were confirmed in all experiments using BBL Dry Anaerobic Indicator Strips (Becton Dickinson Ref: 271051).

Influenza A virus infection

Blvra$^{+/+}$ and *Blvra*$^{-/-}$ mice were maintained at the GIMM BSL-2 facility, and infected with influenza A/X-31, essentially as described (*76, 77*). Briefly, mice were anesthetized with isoflurane and 30µL of inoculum (10^3 PFU in sterile PBS), administered intranasally. Mice were monitored daily, as described above. Viral loads were determined at day 3 post-infection from the right lower lobes of influenza A virus-infected mice. Samples were homogenized in serum-free DMEM (Gibco) using tungsten carbide beads (Qiagen) in a TissueLyser II (Qiagen) at 20 s^{-1} for 3 min and supernatants were collected after centrifugation. Titration by plaque assay was performed as previously described using Madin-Darby Canine Kidney cells (*76*).

UnaG protein synthesis and purification

UnaG was expressed in pMAL-6P2-6xHIS in BL21(DE3) cells (*22*). Starter cultures were grown to saturation in Luria Broth (LB) (overnight at 37°C), diluted 10-fold in LB and grown to an OD600 of 0.3 at 37°C, after which cultures were moved to 18°C. UnaG expression was induced at OD600 of 0.6, by the addition of 400 μM isopropyl β-D-1-thiogalactopyranoside (16h, 18°C). Cells were harvested by centrifugation (3,800 *g*, 4°C, 25 min), resuspended in 15 mL of resuspension buffer (50 mM HEPES, 300 mM NaCl, 0.5 mM TCEP, 10% glycerol, 1 mM PMSF, 2.34 μM leupeptin, 1.45 μM pepstatin at pH 7.4) *per* liter of culture. The sample was further lysed by sonication (QSonica Sonicator) with an amplitude of 5% in a pulse mode of 0.8sec ON and 0.5sec OFF for total 30 sec. Lysate was clarified by centrifugation (26,000 *g*, 4°C, 30 min) and loaded onto an amylose column (MBPTrap™ HP Column, GE Healthcare). Protein was eluted with 20 mM maltose in protease buffer (50 mM Tris, 150 mM NaCl, 0.5 mM TCEP, 10% glycerol, 0.01% TritonX-100 at pH 7.4). MBP was removed by the addition (16h, 4°C) of PreScission Protease (GE Healthcare). UnaG was purified via a nickel column (HisTrap™ HP Column, GE Healthcare) to remove the cleaved tag and eluted with (30 mM Tris, 1M NaCl, 0.5 mM TCEP, 10% glycerol, 500mM imidazole, pH 7.4). UnaG was further purified on a gel-filtration column (S-200, GE Healthcare) in gel filtration buffer (50 mM HEPES, 300 mM NaCl, 0.5 mM TCEP, 10% glycerol at pH 7.4), concentrated using 10kDa amicon ultracentrifugal filter (Merck), and flash frozen in gel filtration buffer at 30% glycerol for storage at −80°C.

UnaG-based assay for quantification of unconjugated bilirubin

Blood from *Blvra*$^{+/+}$ and *Blvra*$^{-/-}$ mice was obtained from the submandibular (facial) vein, before (Day 0) and after (Days 4, 7, 15 and 25) *Pcc* infection. Samples were collected in the dark, under

a red light, immediately centrifuged (1,000 *g*, 15 min.) and plasma was collected, frozen in liquid nitrogen and stored at -80ºC until used for bilirubin quantification. Total plasma unconjugated bilirubin was determined using UnaG (*78*). Plasma sample from human patients or mice non-infected or infected with *Pcc* was diluted 1:100 in PBS. 100 pM of UnaG was added to the diluted plasma sample and incubated for 10 min at RT. After incubation, fluorescence intensity was measured at excitation λ_{480} nm and emission λ_{530} nm using microplate reader (Promega GloMax®). Unconjugated bilirubin (Frontier Chemicals) was used as standard.

Clinical quantification of unconjugated bilirubin

Clinical routine bilirubin measurements were performed at accredited laboratories at Charité – Universitätsmedizin Berlin and Centre de Recherches Médicales de Lambaréné, Gabon, using the modified colorimetric Diazo method (*79*) as implemented by Roche Diagnostics. In brief, bilirubin reacts with 3,5-dichlorophenyldiazonium salt to form azobilirubin. The red color intensity of azobilirubin is directly proportional to bilirubin concentrations. For measurement of total bilirubin, an accelerator is added to the sample to solubilize albumin-bound unconjugated bilirubin before adding the salt, allowing for photometric measurement of total bilirubin (i.e., conjugate and unconjugated bilirubin). Unconjugated bilirubin concentrations are calculated by subtracting conjugate from total bilirubin.

iRFP synthesis and purification

The iRFP gene (Addgene plasmid #31857) was subcloned into pGEX-6P-2 (GE Healthcare Life Sciences) expression vector (*22*) and subsequently transformed into BL21(DE3) cells for protein expression. Starter cultures were grown to saturation in Luria Broth (LB) (overnight at 37°C), diluted 10-fold in LB and grown to an OD600 of 0.3 at 37°C, after which cultures were moved to

18°C. iRFP expression was induced at OD600 of 0.6, by the addition of 400μM isopropyl β-D-1-thiogalactopyranoside (16h, 18°C). Cells were harvested by centrifugation (3,800 *g*, 4°C, 25 min), resuspended (15 mL; 50 mM HEPES, 300 mM NaCl, 0.5 mM TCEP, 10% glycerol, 1 mM PMSF, 2.34 μM leupeptin, 1.45 μM pepstatin; pH 7.4) *per* liter of culture. The sample was further lysed by sonication (QSonica Sonicator) with an amplitude of 5% in a pulse mode of 0.8sec ON and 0.5sec OFF for total 30 sec. Lysate was clarified by centrifugation (26,000 *g*, 4°C, 30 min.) and loaded onto GST column (GSTrap™ Column, GE Healthcare). Protein was eluted with 10mM glutathione in protease buffer (50 mM Tris, 150 mM NaCl, 0.5 mM TCEP, 10% glycerol, 0.01% TritonX-100 at pH 7.4). GST was removed by the addition of PreScission Protease (GE Healthcare) for 16 h at 4°C. iRFP was further purified on a gel-filtration column (S-200, GE Healthcare) in gel filtration buffer (50 mM HEPES, 300 mM NaCl, 0.5 mM TCEP, 10% glycerol at pH 7.4), concentrated using 10kDa amicon ultracentrifugal filter (Merck), and flash frozen in gel filtration buffer at 30% glycerol for storage at −80°C.

iRFP-based assay for quantification of biliverdin

Blood was harvested from the submandibular (facial) vein of *Blvra*$^{+/+}$ and *Blvra*$^{-/-}$ mice, before (Day 0) and after (Days 4, 7 and 15) *Pcc* infection. Plasma was collected in the dark, under a red light, immediately after centrifugation (1,000 *g*, 15 min.), frozen in liquid nitrogen and stored at -80ºC until used. Biliverdin concentration in plasma was quantified using biliverdin-inducible infrared fluorescent protein (iRFP) (*25*). Briefly, plasma samples were diluted (1:100 in PBS) and incubated with iRFP (87 nM; 15min at RT). Fluorescence intensity was measured at excitation λ_{690} nm and emission λ_{713} nm using a microplate reader (BioTek Synergy H1). Biliverdin hydrochloride (Frontier Chemicals) was used as standard.

Bilirubin and biliverdin

For the *in vitro* studies, stock solution (34 mM) of high purity bilirubin and biliverdin (Frontier Scientific, Inc. Logan, Ut, USA) were dissolved in DMSO (Sigma-Aldrich) and protected from light. Stock solutions were further diluted (1mM) in RPMI 1640 supplemented with lipid-rich bovine serum albumin (0.5% AlbuMAXII; Invitrogen™, Thermo Fisher Scientific). Albumin concentration in the culture medium was 75 µM. Unconjugated bilirubin was added to RBC or *P. falciparum* iRBC in culture medium (40, 80 and 120 µM) corresponding to 15, 25 and 41 µM of unconjugated bilirubin, as quantified within 2 hours using a UnaG-based assay (see above) (*21, 22*).

Plasmodium falciparum in vitro culture

Plasmodium falciparum 3D7-GFP (*Pf*3D7-GFP; MRA-1029, MR4, ATCC® Manassas Virginia; chloroquine and artemisinin-sensitive), Dd2 (*Pf*-Dd2; MRA-150, MR4, ATCC® Manassas Virginia; chloroquine-resistant), IPC 5202 (Pf5202; MRA-1240, MR4, ATCC® Manassas Virginia; artemisinin-resistant) and *Plasmodium falciparum* D10 (*Pf*D10; atovaquone-sensitive) and its transgenic derivative (*Pf*D10^{TgDHODH}) (*42*) were co-cultured (37°C; 95% humidity, 5% of CO_2) with human RBC from healthy donors (5% hematocrit), replacing human serum by 0.5% AlbuMAXII (Invitrogen™, Thermo Fisher Scientific), as described (*31, 80*). Cultures were synchronized using 5% D-Sorbitol (Sigma-Aldrich). After RBC reinvasion, the parasites at the schizont stage were suspended, layered onto 70% Percoll (Sigma-Aldrich), centrifuged (1,000g; 15 min.; no brake), collected from the upper layer of Percoll cell suspension, washed (PBS 1X) and incubated in standard culture conditions until RBC reinvasion (*81*). Ring stage (approximately 10-12h after RBC invasion) or trophozoite (approximately 18-20h after RBC invasion) stage parasites were diluted to approximately 1% parasitemia and 3% hematocrit in

RPMI 1640 complete medium, (75µM bovine serum albumin), seeded on a 96-well plate and exposed to vehicle (DMSO; represented in figures as 0 µM bilirubin/biliverdin) or different concentrations of bilirubin (15-41 µM, diluted in DMSO), biliverdin or water soluble bilirubin ditaurate (40-120 µM; Frontier Specialty Chemicals Inc.) for 24, 48 and 72h. Parental *Pf*D10 and its transgenic derivative *Pf*D10^{TgDHODH} were also treated with atovaquone (10 nM; Sigma-Aldrich) for the same period of time. Final DMSO concentration was always kept below 0.5%. Slides were prepared at 24, 48 and 72h and stained with Giemsa solution. In parallel, parasites were suspended (PBS 1X) and analyzed by flow cytometry (Beckman Coulter CytoFLEX) to determine the percentage of iRBC. *Pf*Dd2 and *Pf*5202 parasites were stained with 0.5X SYBR green I (Invitrogen, Thermo Fisher Scientific) and *Pf*D10 and *Pf*D10^{TgDHODH} parasites with 0.5X SYTO Deep Red Nucleic Acid Stain (Invitrogen, Thermo Fisher Scientific) in PBS (45 min. in the dark; 37°C) and washed in PBS prior to acquisition. *Pf*3D7-GFP parasites were acquired directly (GFP^+ signal). Representative Giemsa-stained thin blood smear images were acquired as described for *Pcc.*

Hemolysis assay

*Pf*3D7 parasites cultured in 96-well plates, were synchronized and ring stages (~1% parasitemia, 3% hematocrit) were treated with different concentrations of bilirubin, as described above. At 72h after treatment, 96-well plates were centrifuged (300 *g*, 5min.), supernatants were collected and stored at 4ºC and parasitemias were quantified by flow cytometry as described above. 2% Triton X-100 was used as a positive control to establish 100% RBC lysis. LDH release into the medium was quantified using the LDH-GloTM Cytotoxicity assay (Promega, #J2380). Briefly, culture medium was diluted in LDH Storage Buffer (200mM Tris-HCl, pH 7.3, 10% Glycerol, 1% BSA) to reach a 5X dilution. LDH detection reagent (50µL of LDH detection enzyme mix +

0,25µL Reductase Substrate) was added to each sample (1:1 ratio), incubated (60 min.; RT) and the luminescence was recorded using the GloMax microplate reader (Promega). The percentage of cytotoxicity was calculated using the following formula: (Experimental LDH release – medium background)/(Maximum LDH release control – medium background) x 100.

RNA extraction and qRT-PCR

Mice were sacrificed by CO_2 asphyxiation, transcardially perfused *in toto* with ice-cold PBS (1X, 15 mL) and organs were harvested, snap frozen in liquid nitrogen and stored at -80°C. Total RNA was extracted using tripleXtractor reagent (GRISP), chloroform, isopropanol, and ethanol, according to manufacturer's instructions. cDNA was synthesized using the Xpert cDNA Synthesis Mastermix (GRiSP), followed by qRT-PCR using the iTaq Universal SYBR Green Supermix (Bio-Rad) on a QuantStudio™ 7 Flex Real-Time PCR System (Applied Biosystems). Transcript values were calculated from the threshold cycle (Ct) of each gene using the $2^{-\Delta\Delta CT}$ method using Acidic ribosomal phosphoprotein P0 (*Arbp0*) as the housekeeping control gene. Primers for qPCR include: *Arbp0*, Fwd: 5'-CTTTGGGCATCACCACGAA-3', Rev: 5'-GCTGGCTCCCACCTTGTCT-3'; *Blvra*-deletion confirmation, Fwd: 5′-AGCCGCTGGTAAGCTCC-3′, Rev: 5′-ACCAACCACTACCACACCAAA-3′; *Blvra*, Fwd: 5'-ATTCTGCCACCATGGAAA-3', Rev: 5'-CTCCAAGGACCCAGATTTGA-3'; *Hmox1,* Fwd: 5'-TGACACCTGAGGTCAAGCAC-3', Rev: 5'-TCTCTGCAGGGGCAGTATCT-3'; *Ugt1a1,* Fwd: 5'-TCTGGCTGATGAGAAGTGACT-3'; Rev: 5'-GAAAACAACGATGCCATGCT-3'; *Pcc* AS 18S rRNA, Fwd: 5'- AAGCATTAAATAAAGCGAATACATCCTTAT-3', Rev: 5'-GGGAGTTTGGTTTTGACGTTTATGCG-3'.

Flow cytometry (Plasmodium falciparum)

*Pf*3D7-GFP cultures were synchronized as described before. Ring stage (approximately 10-12h after invasion) or trophozoite stage (approximately 18-20h after invasion) parasites (approximately, 3% parasitemia) were treated with vehicle (0.12-0.47% vol/vol DMSO) or different concentrations of unconjugated bilirubin (15-41 μM) or biliverdin (40-120 μM) for 24h, collected, washed with 1X PBS and stained as previously described (*31*). Cells were stained with MitoTracker™ Green FM (200 nM in 1X PBS; Invitrogen™, Thermo Fisher Scientific), MitoTracker™ Deep Red FM (200 nM in 1X PBS; Invitrogen™, Thermo Fisher Scientific), and MitoSOX™ Red Mitochondrial Superoxide Indicator (5 μM in 1X PBS; Invitrogen™, Thermo Fisher Scientific) for 20 min., 37ºC, 5% CO_2. Cells were washed once with 1X PBS and stained with Hoechst 33342 (10 μM in 1X PBS; Thermo Fisher Scientific) for 20 min., 37ºC, 5% CO_2. Cells were again washed once with 1X PBS and analyzed in a FACSAria™ Ilu Cell Sorter (BD Biosciences). FACS data was analyzed with FlowJo V10.8.1. Gating strategy illustrated in **Data S1-2**.

Western blot

Mice were sacrificed by CO_2 asphyxiation, transcardially perfused *in toto* with ice-cold PBS (1X, 15 mL) and organs were harvested and stored at -80ºC. Tissues were lysed in 2% SDS-PAGE sample buffer (100 mM Tris, pH 6.8, 20% glycerol, 4% SDS, 0.2% bromophenol blue, 100mM DTT) supplemented with 1X protease inhibitor cocktail (cOmplete™, Mini, EDTA-free Protease Inhibitor Cocktail; Roche) and homogenized in a TissueLyser II (Qiagen) with tungsten carbide beads (Qiagen). Supernatants were collected, boiled (5 min., 95ºC) and total protein was quantified at λ_{280} nm using the DS-11 FX Spectrophotometer (DeNovix). Proteins (50 or 150μg) were resolved on a 12% SDS-PAGE and transferred to Polyvinylidene fluoride (PVDF)

membranes. Membranes were blocked (1h at RT; 5% milk in 1X TBS-T), washed (1X TBS-T) and incubated (overnight at 4°C) with primary antibodies (5% BSA in 1X TBS-T): rabbit polyclonal anti-BVRA (Invitrogen, ThermoFisher Scientific, PA5-92059; 1:1000), rabbit polyclonal anti-HO-1 (Enzo Life Sciences, ADI-SPA-896F; 1:1000), rabbit monoclonal anti-GAPDH (Cell Signaling Technology, clone 14C10, #2118; 1:1000) and rabbit polyclonal anti-β-actin (Cell Signaling Technology, #4967; 1:1000). Membranes were washed (3 times in 1X TBS-T) and incubated (2h; RT) with the peroxidase-conjugated secondary antibody (HRP conjugated goat anti-rabbit IgGH+L; Invitrogen, #31460; 1:5000; 5% milk in 1X TBS-T). Membranes were washed (3 times in 1X TBS-T) and peroxidase activity was detected using SuperSignal™ West Pico PLUS Chemiluminescent Substrate (ThermoFisher Scientific). Blots were developed using Amersham Imager 680 (GE Healthcare), equipped with a Peltier cooled Fujifilm Super CCD. Western blot analysis was performed using ImageJ (Rasband, W.S., ImageJ, U.S. NIH, Bethesda, Maryland, USA, https://imagej.nih.gov/ij/,1997-2014), from images without saturated pixels. Uncropped Western blot membranes are shown in **Data S3**. For hepatic UGT1A1 detection the procedure was modified as follows: tissues were lysed using radioimmunoprecipitation assay (RIPA) buffer (pH 7.5) (50mM TrisHCl, 1% NP40, 0,25% deoxycholic acid, 150mM NaCl, 1mM EGTA, 1mM Sodium Orthovanadate, 1mM Sodium Fluoride and 1X protease inhibitor cocktail (cOmplete™, Mini, EDTA-free Protease Inhibitor Cocktail; Roche) and homogenized in a TissueLyser II (Qiagen) with tungsten carbide beads (Qiagen). Samples were centrifuged (15000 g 15min., 4°C), the supernatants were collected, and the total protein concentration was quantified by the Bradford assay, according to the manufacturer instructions (Bio-rad Protein Assay Dye Reagent Concentrate, #5000006). Protein (40µg) were resolved on a 10% SDS-PAGE and transferred to Polyvinylidene fluoride (PVDF) membrane. The membrane was blocked (2h at RT; 5% milk in 1X PBS-T) and incubated with

rabbit polyclonal anti-UGT1A1 (Boster Biological Technology, A01865-1; 1:1000). The membrane was washed (3 times in 1X-PBS-T) and incubated (1h, RT) with the peroxidase-conjugated secondary antibody (HRP conjugated goat anti-rabbit IgGH+L; Invitrogen, #31460; 1:5000; 5% milk in 1X PBS-T). The membrane was washed (3 times in 1X-PBS-T) and the peroxidase activity was detected as described above.

High-pressure freezing (HPF), freeze substitution and Transmission Electron Microscopy

*Pf3*D7-GFP cultures were synchronized as described (*81*). Trophozoite stage parasites (approximately 18-20h after invasion, 4-5% parasitemia) were treated with vehicle (0.35% vol/vol DMSO) or bilirubin (41 μM) or biliverdin (120 μM) for 8 or 12h, collected and fixed overnight at 4ºC with 1% (v/v) glutaraldehyde (Science Services) in 0.1M cacodylate buffer (Sigma-Aldrich) with 1 mM $CaCl_2$ (Alfa Aesar) and 3 mM $MgCl_2$ (Alfa Aesar). Parasites were pelleted by centrifugation (300 *g*; 5 min.), washed 3 times in 0.1M cacodylate buffer (Sigma-Aldrich) (pH 7.2), mixed in RPMI medium containing 20% (w/v) polyvinylpyrrolidone 40 (Sigma-Aldrich) as a cryoprotectant and high-pressure-frozen using a High-Pressure Freezer Compact 02 (Wohlwend Engineering Switzerland). The samples were freeze-substituted using a Leica AFS2 equipped with a Leica EM FSP Robot with 0.2% (w/v) uranyl acetate (Analar) in acetone during 1h at -140ºC, followed by an increasing slope of 4ºC/h until -90ºC and then samples were substituted for 6h at -90°C. The temperature was raised to -50ºC at a slope of 5ºC/h and the samples were washed three times in acetone for 1h each ste*P.* Samples were then infiltrated in Lowicryl HM20 resin (Polysciences) at increasing concentrations of 33, 66 and 100% and polymerized with UV light at -30ºC for 72h after a slope of 5ºC/h. Sections of 70 nm thickness were cut using a Leica EM UC7 ultramicrotome using an Ultra 45° diamond knife (Diatome) and mounted on palladium-copper 1x2mm slot grids coated with 1% (w/v) formvar

(Agar Scientific) in chloroform (VWR). Sections were stained with 2% (w/v) uranyl acetate (Analar) in 70% methanol (VWR) and Reynold's lead citrate (Sigma-Aldrich; 5min. each) and analyzed using a Tecnai G^2 Spirit BioTWIN Transmission Electron Microscope from FEI operating at 120 kV and equipped with an Olympus-SIS Veleta CCD Camera.

Scanning Electron Microscopy

Vehicle (0.35% vol/vol DMSO) or bilirubin (41 μM) was added to the culture medium used to culture *Pf*D7-GFP for 12h. The samples were collected, centrifuged (500 *g*, 5 min) and washed (3X in 100 mM $NaHCO_3$, pH 9.0 and 2% SDS; 11,000 *g*, 30 min; and 5X in distilled H2O to remove the salts and detergents (4 times 11,000 *g*,10 min and the last wash 11,000 *g*, 30 min). Samples were stored in 200 μL of distilled H_2O at 4°C until processing. 20 μL of each sample were added to a silicon wafer and allowed to air dry. Before analysis, samples were coated with gold for 5 seconds. Samples were imaged in a Quanta 650 FEG Scanning Electron Microscope from FEI operating at 5 kV.

Single-cell RNA sequencing

Single-cell RNA sequencing was performed essentially as described (*31, 32*). Briefly, *Blvra*$^{+/+}$ and *Blvra*$^{-/-}$ mice were sacrificed by CO_2 asphyxiation 7 days after *Pcc* AS-GFP infection (*i.e.,* peak of infection) and the blood was collected by cardiac puncture. The blood was diluted 1:75 in 1X PBS supplemented with 1 % FBS and iRBC (GFP^+ cells) were sorted on a BD FACSAria Ilu. Cells were washed twice with 1X PBS supplemented with 1 % FBS and adjusted to a concentration of 1200 cells/mL.

Single-cell gene expression library preparation and sequencing

Library preparation and sequencing was performed essentially as previously described (*31, 32*). Briefly, samples were processed with Chromium Single Cell Controller to generate barcoded single-cell gel bead emulsions (GEMs) following the Chromium Next GEM Single Cell 3′ protocol. Single-cell cDNA libraries were obtained after the GEM-RT (reverse-transcriptase) clean-up and cDNA amplification on a Bio-Rad C1000 Touch Thermal Cycler. The cDNA profiles were checked on a Fragment Analyzer System (Agilent Technologies) according to the HS NGS Fragment kit (Agilent Technologies) manual. The scRNA-seq libraries were generated and indexed (Dual Index Plate TT, Set A) on a Bio-Rad C1000 Touch Thermal Cycler. The final 3' Gene Expression libraries were verified and quantified on a Fragment Analyzer System (Agilent Technologies) following the HS NGS Fragment kit (Agilent Technologies) and samples were sequenced on a NextSeq 2000 (Illumina) using the NextSeq 1000/2000 P2 kit 100 cycles (Read 1: 28 Cycles; Read 2: 90 cycles).

Single-cell RNA-seq data analysis

Single-cell analyses were performed with Seurat (v.4.3.0) (*82-84*) and scuttle (v1.2.1) (*85*). Cells expressing less than 200, more than 1,500 genes, or more than 4,000 UMIs were filtered out. Remaining cells were annotated by projection to the malaria cell atlas, *P. falciparum* 10x set 4 (https://www.malariacellatlas.org/data-sets/) (*86*) using scmap (v1.14.0) (*87*) through 1:1 orthologs downloaded on 18.01.2024 from PlasmoDB (https://plasmodb.org/plasmo/app/search/transcript/GenesByOrthologPattern). The atlas and query samples were subset to the 1:1 ortholog gene set and log1p normalized. A cell index of the atlas was built using 500 genes and the cells from the query samples were individually projected using the scmapCell() function. The *Blvra*$^{+/+}$ and *Blvra*$^{-/-}$ samples were individually normalized

with scran (v1.20.1) (*88*) using the quickCluster() method, and integrated using STACAS (v2.0.1) (*89*) with 750 genes and semi-supervised by the scmap projected stages. The integrated data was visualized by projection into UMAP (Uniform Manifold Approximation and Projection) using 8 principal components and the umap-learn method through Seurat. Analysis of differentially expressed genes of *Blvra*$^{-/-}$ *vs*. *Blvra*$^{+/+}$ was performed individually for different stage clusters based on the scmap projection, using the Wilcoxon rank sum test through Seurat. Functional enrichment analysis of significantly (Bonferroni-adjusted $p<0.05$) up- or down-regulated genes was performed using gprofiler2 (v.0.2.2) (*90*). The archived version of the gprofiler2 server - Ensembl 108, Ensembl Genomes 55 (database built on 2022-12-28) was used: https://biit.cs.ut.ee/gprofiler_archive3/e108_eg55_p17/gost. All the analyses were performed with the R programming language in a containerized docker image publicly available at Docker Hub (*elolabfi/sctoolkit*) running R (v.4.2.1) (R Core Team, 2021) (*91*), RStudio server (2022.07.2 Build 576), Seurat (v.4.3.0) and its dependencies. RNA velocity was performed with velocyto (v.0.17.17) (*92*) and scvelo (v.0.2.5) (*33*) as described in (Ref. (*32*)) with python (v.3.9.5) run under Jupyter lab (v.3.5.3). All the data is available in **Data tables S1-4**.

Live cell imaging and confocal microscopy

*Pf*3D7 cultures were synchronized, as described above and ring (10-12h after RBC invasion) or trophozoite (18-20h after invasion) stage parasites (3% parasitemia) were incubated with vehicle (0.35% vol/vol DMSO), unconjugated bilirubin (41 µM) or biliverdin (120 µM). RBC were harvested 12h or 24h for food vacuole and Hz or mitochondrion analyses, respectively. Cells were washed (1X PBS; 400 *g*, 2 min.) and stained (30 min., RT) with MitoTracker™ Green FM (200 nM in 1X PBS; Invitrogen™) or LysoTracker™ Green DND-26 (75 nM in 1X PBS; Invitrogen™), Hoechst 33342 (20 µM in 1X PBS) and Wheat Germ Agglutinin (WGA) Alexa

Fluor 633 (3 µg/mL in 1X PBS; Thermo Fisher Scientific). Cells were washed twice (1X PBS; 400 *g*, 2 min.) and the cell pellet was resuspended in 1 mL of PBS. Then, 200 µL of the cell suspension were placed in chambered coverslip with 8 wells and a #1.5H glass bottom (Ibidi GmbH, Munich, Germany). After this step, the cells were analyzed using a laser scanning confocal microscope (Leica TCS-SP5) with a continuous Ar-ion and HeNe and a Ti:sapphire laser (Spectra-Physics Mai Tai BB, 710–990 nm, 100 fs, 82 MHz). Both MitoTracker™ Green FM and LysoTracker™ Green DND-26 were imaged using the 488 nm Ar+ laser line (with emission set at 500-610 nm) and the 633 nm He−Ne laser line was used for imaging WGA-Alexa 633 dye (emission 644-736 nm). Hoechst 33342 images were recorded in the multiphoton mode under 810 nm excitation (420-550 nm), and hemozoin was visualized using the laser reflection mode. Images (512 × 512 pixels) were collected using a 63x 1.2 N.A. water immersion objective (HCX PL APO CS 63.0x 1.20WATERUV) at a scan rate of 100 Hz laser. To measure the relative area and fluorescence intensity corresponding to LysoTracker Green (*i.e.*, food vacuole) or Hz, a line was drawn across the diameter of *P. falciparum* 3D7 infected RBC, intercepting the food vacuole, using ImageJ 1.53k software (Rasband, W.S., ImageJ, U.S. NIH, Bethesda, Maryland, USA, https://imagej.nih.gov/ij/,1997-2014). Relative Intensity and the distance were measured using ImageJ. For LysoTracker Green, Area under the curve (AUC) was calculated from the above values. Values were calculated from 2 independent experiments analyzing 5-7 parasites *per* experiment. To measure the relative area corresponding to MitoTracker Green staining, images were analyzed using Imaris 10.0.0 software. The surface around the MitoTracker Green was created using the Surface Tool in Imaris and the area *per* parasite was measured. Values were calculated from 2 independent experiments analyzing 15-17 parasites *per* experiment.

Hz quantification

Hz was quantified essentially as described (*93, 94*), with the following adaptations. Briefly, blood was obtained by heart puncture, from *Blvra*$^{+/+}$ and *Blvra*$^{-/-}$ mice 7 days after *Pcc* infection. Mice were housed at a regular light cycle: lights on from 8:00 am (Zeitgeber time: ZT 0) to 8:00 pm (ZT 12), or at an inverted light cycle: lights on from 8:00 pm (ZT 0) to 8:00 am (ZT 12). Blood (300-400 µL) was collected at ZT 3 and 15, hypotonically lysed (4 mL H_2O), centrifuged (11,000 *g*, 45 min.). The supernatant fraction was removed, and pellets (Hz) were washed (3X in 100 mM $NaHCO_3$, pH 9.0 and 2% SDS; 11,000 *g*, 30 min.). Hz was dissolved (1 mL of 100 mM NaOH, 2% SDS, 3 mM EDTA), sonicated (1 min. Branson SLPe Digital Sonifier) and centrifuged (11,000 *g*, 30 min.). The heme released from Hz (200 µL) was quantitated by spectrophotometry (405nm) in a 96 well plate reader (MultiscanSky, ThermoFisher) with molar extinction coefficient of 5.7×10^4. Heme concentration was calculated according to the Lambert-Beer law: $A=\varepsilon.c.l$ (A – absorbance at l_{405} nm; ε – extinction coefficient of hemin- 57000; c – concentration in molar (M); l – path length) and normalized to the volume of blood used. Data is presented as Hz (*i.e.*, nM heme).

β-Hematin inhibition assay

The Nonidet P-40 (NP-40) detergent-mediated assay (*47*) adapted for high-throughput screening in 96-well plate was used to determine inhibition of β-hematin formation. Following a period of 4-5h incubation at 37°C, the formation of a *bis*-pyridyl hemochromogen is detectable at a wavelength of 405 nm, and allows quantification of the free heme component that has not reacted to form β-hematin (*95*). Measurements were made using a Thermo Scientific Multiskan GO plate reader. Sigmoidal dose-response curves were plotted in GraphPad Prism to determine

half maximal inhibitory concentration (IC_{50}) values. Measurements were performed twice, each in technical duplicate, and the values are reported together with standard deviation.

Metabolite extraction

*Pf3*D7-GFP cultures were synchronized as described (*81*). Trophozoite stage parasites (approximately 18-20h after invasion, 15% parasitemia, 5% HCT, 2 mL culture *per* sample) and treated with vehicle (0.35% vol/vol DMSO) or bilirubin (41 μM) for 8 or 12h. The chemicals used were LC-MS grade water, acetonitrile (ACN), methanol (MeOH), and isopropanol (IPA), which were obtained from Th. Geyer (Germany). High-purity methyl tert-butyl ether (MTBE), ammonium formate, formic acid, ammonium acetate, and acetic acid were purchased from Merck (Germany). Stable isotope labelled internal standards for metabolomics (MSK-A2-1.2; Cambridge Isotope Laboratories, MA, USA) were used at final concentrations of 1.0% (vol/vol). The culture medium was completely aspirated and the cells were washed with 1XPBS (500 *g*, 5 min). For biphasic extraction of lipids and polar metabolites, samples were initially quenched by incubation on dry ice with 400 μL of 75% (vol/vol) cold methanol for 20 min and the appropriate internal standards (0.5 μL each/sample) were added. After incubation, the samples were vortexed for 5 min at maximum speed, lysed using an ultrasonic bath to sonicate the sample for 5 min and vortexed again briefly after sonication. After addition of 1000 μL of cold MTBE, the monophasic mixture was vortexed for 60 s and incubated at -20°C for 20 min. For phase separation, 250 μL of cold water were added, followed by another vortexing and incubation step (see previous conditions). The biphasic solvent system was then centrifuged for 15 min at 14,000 *g* and 4 °C. For metabolomics analysis, 400 μL of the bottom aqueous phase were transferred, dried under a stream of nitrogen, and reconstituted in 75 μL 80% MeOH (v/v). The final samples

were vortexed for 10 min, centrifuged (see previous conditions) and the supernatants were transferred to analytical glass vials for LC-MS/MS analysis.

LC-MS/MS analysis

LC-MS/MS analysis was performed on a Vanquish Horizon UHPLC system coupled to an Orbitrap Exploris 240 high-resolution mass spectrometer (Thermo Scientific, MA, USA) in negative and positive ESI (electrospray ionization) mode. To perform untargeted metabolomics, chromatographic separation was carried out on an Atlantis Premier BEH Z-HILIC column (Waters, MA, USA; 2.1 mm x 100 mm, 1.7 µm) at a flow rate of 0.25 mL/min. The mobile phase consisted of water:acetonitrile (9:1, v/v; mobile phase phase A) and acetonitrile:water (9:1, v/v; mobile phase B), which were modified with a total buffer concentration of 10 mM ammonium acetate (negative mode) and 10 mM ammonium formate (positive mode), respectively. The aqueous portion of each mobile phase was pH-adjusted (negative mode: pH 9.0 via addition of ammonium hydroxide; positive mode: pH 3.0 via addition of formic acid). The following gradient (20 min total run time including re-equilibration) was applied (time [min]/%B): 0/95, 2/95, 14.5/60, 16/60, 16.5/95, 20/95. Column temperature was maintained at 40°C, the autosampler was set to 4°C and sample injection volume was 5 µL. Analytes were recorded via a full scan with a mass resolving power of 120,000 over a mass range from 60 – 900 m/z (scan time: 100 ms, RF lens: 70%). To obtain MS/MS fragment spectra, data-dependent acquisition was carried out (resolving power: 15,000; scan time: 22 ms; stepped collision energies [%]: 30/50/70; cycle time: 900 ms). Ion source parameters were set to the following values: spray voltage: 4100 V (positive mode) / -3500 V (negative mode), sheath gas: 30 psi, auxiliary gas: 5 psi, sweep gas: 0 psi, ion transfer tube temperature: 350°C, vaporizer temperature: 300°C. All experimental samples were measured in a randomized manner. Pooled

quality control (QC) samples were prepared by mixing equal aliquots from each processed sample. Multiple QCs were injected at the beginning of the analysis in order to equilibrate the analytical system. A QC sample was analyzed after every 5th experimental sample to monitor instrument performance throughout the sequence. For determination of background signals and subsequent background subtraction, an additional processed blank sample was recorded. Data was processed using MS DIAL 4.9.221218 (*96*) and raw peak intensity data was normalized via total ion count of all detected analytes (*97*). Level 1 feature identification was based on an in-house library for metabolomics (EMBL-MCF 2) (*98*) using accurate mass, isotope pattern, MS/MS fragmentation, and retention time information and a minimum matching score of 80%. All the raw data results for annotated metabolites are available in **Data table S5.**

Statistical analysis

For clinical data we used Mann Whitney U test. Analysis was done in JMP Pro version 16 (SAS Institute Inc, Cary, NC, USA). For all other analyses, statistically significant differences between two experimental groups were assessed using a two-tailed unpaired Mann-Whitney U test or t test (in samples tested positive for normal distribution) and comparisons between more than two groups were assessed using one-way ANOVA, two-way ANOVA (parasitemias and parasite burden) or two-way ANOVA with Bonferroni's or Tukey's multiple comparison test. Survival curves are represented by Kaplan-Meier plots and differences between the groups were assessed using the log-rank test. All statistical analyses were performed using GraphPad Prism software. Differences were considered statistically significant at a P value <0.05. NS: not-significant, $p>0.05$; *$p<0.05$; **$p<0.01$; ***$p<0.001$; ****$p<0.0001$.

For *in vivo Plasmodium* infection experiments, sample size was maintained no less than 5 mice *per* experimental condition, in at least 2 independent experiments, except when indicated in the

Figure Legends. For *in vitro* experiments, sample size was maintained no less than 4 replicates *per* experimental condition, in a minimum of 3 independent experiments, except when indicated in the Figure Legends.

Randomization was used in mice monitoring after infection. Samples were analyzed blindly, often being processed by a different investigator from the one preparing/collecting the samples.

Inclusion/exclusion criteria for human studies are detailed in the *Human data* section. For in vivo *Plasmodium* infection experiments, mice presenting a >2 days delay in the initial dynamics of parasite growth and peak of parasitemia were considered as technical outliers and were excluded from further analysis.

References

1. A. M. Dondorp *et al.*, The relationship between age and the manifestations of and mortality associated with severe malaria. *Clinical infectious diseases : an official publication of the Infectious Diseases Society of America* **47**, 151-157 (2008).
2. K. Marsh *et al.*, Indicators of life-threatening malaria in African children. *N Engl J Med* **332**, 1399-1404 (1995).
3. H. Patel, C. Dunican, A. J. Cunnington, Predictors of outcome in childhood Plasmodium falciparum malaria. *Virulence* **11**, 199-221 (2020).
4. R. K. Kutty, M. D. Maines, Purification and characterization of biliverdin reductase from rat liver. *Journal of Biological Chemistry* **256**, 3956-3962 (1981).
5. R. Schmid, L. Hammaker, J. Axelrod, The enzymatic formation of bilirubin glucuronide. *Arch Biochem Biophys* **70**, 285-288 (1957).

6. S. Ramos *et al.*, Targeting circulating labile heme as a defense strategy against malaria. *Life Science Alliance* **7**, e202302276 (2024).

7. P. A. Sigala, D. E. Goldberg, The peculiarities and paradoxes of Plasmodium heme metabolism. *Annu Rev Microbiol* **68**, 259-278 (2014).

8. A. Pamplona *et al.*, Heme oxygenase-1 and carbon monoxide suppress the pathogenesis of experimental cerebral malaria. *Nat Med* **13**, 703-710 (2007).

9. A. Ferreira, J. Balla, V. Jeney, G. Balla, M. P. Soares, A central role for free heme in the pathogenesis of severe malaria: the missing link? *J Mol Med* **86**, 1097-1111 (2008).

10. A. Ferreira *et al.*, Sickle Hemoglobin Confers Tolerance to Plasmodium Infection. *Cell* **145**, 398–409 (2011).

11. Z. Gouveia *et al.*, Characterization of plasma labile heme in hemolytic conditions. *FEBS J* **284**, 3278-3301 (2017).

12. M. P. Soares, M. T. Bozza, Red alert: labile heme is an alarmin. *Curr Opin Immunol* **38**, 94-100 (2016).

13. T. F. Pais *et al.*, Brain endothelial STING1 activation by Plasmodium-sequestered heme promotes cerebral malaria via type I IFN response. *Proc Natl Acad Sci U S A* **119**, e2206327119 (2022).

14. S. Ramos *et al.*, Renal control of disease tolerance to malaria. *Proc Natl Acad Sci U S A* **116**, 5681-5686 (2019).

15. R. Tenhunen, H. S. Marver, R. Schmid, The enzymatic conversion of heme to bilirubin by microsomal heme oxygenase. *Proc Natl Acad Sci U S A* **61**, 748-755 (1968).

16. S. B. Amin, Narrative review of bilirubin measurement and binding. *Pediatric Medicine* **4**, 1-15 (2021).

17. P. J. Bosma *et al.*, Bilirubin UDP-glucuronosyltransferase 1 is the only relevant bilirubin glucuronidating isoform in man. *Journal of Biological Chemistry* **269**, 17960-17964 (1994).

18. D. G. Levitt, M. D. Levitt, Quantitative assessment of the multiple processes responsible for bilirubin homeostasis in health and disease. *Clin Exp Gastroenterol* **7**, 307-328 (2014).

19. P. J. Bosma *et al.*, The genetic basis of the reduced expression of bilirubin UDP-glucuronosyltransferase 1 in Gilbert's syndrome. *N Engl J Med* **333**, 1171-1175 (1995).

20. N. Guirguis, A. X. Bertrand, C. F. Rose, S. Matoori, 175 Years of Bilirubin Testing: Ready for Point-of-Care? *Adv Healthc Mater* **12**, e2203380 (2023).

21. A. Kumagai *et al.*, A bilirubin-inducible fluorescent protein from eel muscle. *Cell* **153**, 1602-1611 (2013).

22. C. Vasavda *et al.*, Bilirubin Links Heme Metabolism to Neuroprotection by Scavenging Superoxide. *Cell Chem Biol* **26**, 1450-1460 e1457 (2019).

23. S. Kumar *et al.*, Bilirubin inhibits Plasmodium falciparum growth through the generation of reactive oxygen species. *Free Radic Biol Med* **44**, 602-613 (2008).

24. R. Stephens, R. L. Culleton, T. J. Lamb, The contribution of Plasmodium chabaudi to our understanding of malaria. *Trends Parasitol* **28**, 73-82 (2012).

25. A. Berlec, B. Štrukelj, A high-throughput biliverdin assay using infrared fluorescence. *J Vet Diagn Invest* **26**, 521-526 (2014).

26. E. Seixas *et al.*, Heme oxygenase-1 affords protection against noncerebral forms of severe malaria. *Proc Natl Acad Sci U S A* **106**, 15837-15842 (2009).

27. G. Bortolussi *et al.*, CRISPR-Cas9-mediated somatic correction of a one-base deletion in the Ugt1a gene ameliorates hyperbilirubinemia in Crigler-Najjar syndrome mice. *Molecular Therapy - Methods & Clinical Development* **31**, 101161 (2023).

28. J. Jacobsen, R. Brodersen, Albumin-bilirubin binding mechanism. *J Biol Chem* **258**, 6319-6326 (1983).

29. S. D. Zucker, W. Goessling, A. G. Hoppin, Unconjugated bilirubin exhibits spontaneous diffusion through model lipid bilayers and native hepatocyte membranes. *J Biol Chem* **274**, 10852-10862 (1999).

30. S. K. Dogga *et al.*, A single cell atlas of sexual development in Plasmodium falciparum. *Science* **384**, eadj4088 (2024).

31. S. Ramos *et al.*, A hypometabolic defense strategy against malaria. *Cell Metab* **34**, 1183-1200.e1112 (2022).

32. E. Jentho *et al.*, Single-cell RNA sequencing and analysis of rodent blood stage Plasmodium. *STAR Protoc* **4**, 102491 (2023).

33. V. Bergen, M. Lange, S. Peidli, F. A. Wolf, F. J. Theis, Generalizing RNA velocity to transient cell states through dynamical modeling. *Nat Biotechnol* **38**, 1408-1414 (2020).

34. P. J. Spence *et al.*, Vector transmission regulates immune control of Plasmodium virulence. *Nature* **498**, 228-231 (2013).

35. X. Y. Yam *et al.*, Characterization of the Plasmodium Interspersed Repeats (PIR) proteins of Plasmodium chabaudi indicates functional diversity. *Scientific Reports* **6**, 23449 (2016).

36. J. Lawton *et al.*, Characterization and gene expression analysis of the cir multi-gene family of plasmodium chabaudi chabaudi (AS). *BMC Genomics* **13**, 125 (2012).

37. T. D. Otto *et al.*, A comprehensive evaluation of rodent malaria parasite genomes and gene expression. *BMC Biology* **12**, 86 (2014).

38. T. Brugat *et al.*, Antibody-independent mechanisms regulate the establishment of chronic Plasmodium infection. *Nature Microbiology* **2**, 16276 (2017).

39. V. A. Najjar, B. Childs, The crystallization and properties of serum bilirubin. *J Biol Chem* **204**, 359-366 (1953).

40. E. Alves *et al.*, Biliverdin targets enolase and eukaryotic initiation factor 2 (eIF2alpha) to reduce the growth of intraerythrocytic development of the malaria parasite Plasmodium falciparum. *Sci Rep* **6**, 22093 (2016).

41. I. W. Sherman, Biochemistry of Plasmodium (malarial parasites). *Microbiol Rev* **43**, 453-495 (1979).

42. H. J. Painter, J. M. Morrisey, M. W. Mather, A. B. Vaidya, Specific role of mitochondrial electron transport in blood-stage Plasmodium falciparum. *Nature* **446**, 88-91 (2007).

43. I. K. Srivastava, H. Rottenberg, A. B. Vaidya, Atovaquone, a broad spectrum antiparasitic drug, collapses mitochondrial membrane potential in a malarial parasite. *J Biol Chem* **272**, 3961-3966 (1997).

44. A. U. Orjih, H. S. Banyal, R. Chevli, C. D. Fitch, Hemin lyses malaria parasites. *Science* **214**, 667-669 (1981).

45. K. A. de Villiers, T. J. Egan, Heme Detoxification in the Malaria Parasite: A Target for Antimalarial Drug Development. *Acc Chem Res* **54**, 2649-2659 (2021).

46. S. Pagola, P. W. Stephens, D. S. Bohle, A. D. Kosar, S. K. Madsen, The structure of malaria pigment beta-haematin. *Nature* **404**, 307-310 (2000).

47. M. D. Carter, V. V. Phelan, R. D. Sandlin, B. O. Bachmann, D. W. Wright, Lipophilic mediated assays for beta-hematin inhibitors. *Comb Chem High Throughput Screen* **13**, 285-292 (2010).

48. A. F. Slater, A. Cerami, Inhibition by chloroquine of a novel haem polymerase enzyme activity in malaria trophozoites. *Nature* **355**, 167-169 (1992).

49. J. A. Bonilla, T. D. Bonilla, C. A. Yowell, H. Fujioka, J. B. Dame, Critical roles for the digestive vacuole plasmepsins of Plasmodium falciparum in vacuolar function. *Mol Microbiol* **65**, 64-75 (2007).

50. J. M. Matz, Plasmodium's bottomless pit: properties and functions of the malaria parasite's digestive vacuole. *Trends Parasitol* **38**, 525-543 (2022).

51. R. Stocker, Y. Yamamoto, A. F. McDonagh, A. N. Glazer, B. N. Ames, Bilirubin is an antioxidant of possible physiological importance. *Science* **235**, 1043-1046 (1987).

52. L. Vitek, T. D. Hinds, Jr., D. E. Stec, C. Tiribelli, The physiology of bilirubin: health and disease equilibrium. *Trends Mol Med* **29**, 315-328 (2023).

53. A. C. ANAND, P. PURI, Jaundice in malaria. *Journal of Gastroenterology and Hepatology* **20**, 1322-1332 (2005).

54. E. Beutler, T. Gelbart, A. Demina, Racial variability in the UDP-glucuronosyltransferase 1 (UGT1A1) promoter: a balanced polymorphism for regulation of bilirubin metabolism? *Proc Natl Acad Sci U S A* **95**, 8170-8174 (1998).

55. P. Solé-Navais *et al.*, Genome-wide analyses of neonatal jaundice reveal a marked departure from adult bilirubin metabolism. *Nature Communications* **15**, 7550 (2024).

56. C. P. Strassburg, Gilbert-Meulengracht's syndrome and pharmacogenetics: is jaundice just the tip of the iceberg? *Drug Metab Rev* **42**, 168-181 (2010).

57. M. Jallow *et al.*, Genome-wide and fine-resolution association analysis of malaria in West Africa. *Nature Genetics* **41**, 657-665 (2009).

58. C. Timmann *et al.*, Genome-wide association study indicates two novel resistance loci for severe malaria. *Nature* **489**, 443-446 (2012).

59. G. Band *et al.*, A novel locus of resistance to severe malaria in a region of ancient balancing selection. *Nature* **526**, 253-257 (2015).

60. M. Ravenhall *et al.*, Novel genetic polymorphisms associated with severe malaria and under selective pressure in North-eastern Tanzania. *PLoS Genet* **14**, e1007172 (2018).

61. G. Band *et al.*, Insights into malaria susceptibility using genome-wide data on 17,000 individuals from Africa, Asia and Oceania. *Nature Communications* **10**, 5732 (2019).

62. S. D. Zucker, W. Goessling, J. L. Gollan, Kinetics of bilirubin transfer between serum albumin and membrane vesicles. Insight into the mechanism of organic anion delivery to the hepatocyte plasma membrane. *J Biol Chem* **270**, 1074-1081 (1995).

63. S. Kreimendahl, L. Pernas, Metabolic immunity against microbes. *Trends Cell Biol* **34**, 496-508 (2024).

64. S. C. Stearns, R. Medzhitov, *Evolutionary Medicine*. (Oxford University press, ed. 1st Edition, 2015).

65. G. Bancone *et al.*, Contribution of genetic factors to high rates of neonatal hyperbilirubinaemia on the Thailand-Myanmar border. *PLOS Glob Public Health* **2**, e0000475 (2022).

66. P. A. Dennery, D. S. Seidman, D. K. Stevenson, Neonatal hyperbilirubinemia. *N Engl J Med* **344**, 581-590 (2001).

67. S. M. Riordan, S. M. Shapiro, Review of bilirubin neurotoxicity I: molecular biology and neuropathology of disease. *Pediatr Res* **87**, 327-331 (2020).

68. D. P. Kwiatkowski, How malaria has affected the human genome and what human genetics can teach us about malaria. *Am J Hum Genet* **77**, 171-192 (2005).

69. B. O. Olusanya, S. Teeple, N. J. Kassebaum, The Contribution of Neonatal Jaundice to Global Child Mortality: Findings From the GBD 2016 Study. *Pediatrics* **141**, 496-508 (2018).

70. W. C. Golden, The African-American neonate at risk for extreme hyperbilirubinemia: a better management strategy is needed. *Journal of Perinatology* **37**, 321-322 (2017).

71. G. R. C. Global Malaria Programme (GMP), W. H. Organization, Ed. (2013), pp. 451.

72. P. A. Harris *et al.*, Research electronic data capture (REDCap)—A metadata-driven methodology and workflow process for providing translational research informatics support. *Journal of Biomedical Informatics* **42**, 377-381 (2009).

73. S. E. Reece, J. Thompson, Transformation of the rodent malaria parasite Plasmodium chabaudi and generation of a stable fluorescent line PcGFPCON. *Malaria Journal* **7**, 183 (2008).

74. B. Wegiel *et al.*, Cell surface biliverdin reductase mediates biliverdin-induced anti-inflammatory effects via phosphatidylinositol 3-kinase and Akt. *J Biol Chem* **284**, 21369-21378 (2009).

75. S. Weis *et al.*, Metabolic adaptation establishes disease tolerance to sepsis. *Cell* **169**, 1263–1275 (2017).

76. T. A. Etibor *et al.*, Defining basic rules for hardening influenza A virus liquid condensates. *eLife* **12**, e85182 (2023).

77. N. B. Santos, Z. E. Vaz da Silva, C. Gomes, C. A. Reis, M. J. Amorim, Complement Decay-Accelerating Factor is a modulator of influenza A virus lung immunopathology. *PLoS Pathog* **17**, e1009381 (2021).

78. S. Iwatani *et al.*, Fluorescent protein-based detection of unconjugated bilirubin in newborn serum. *Sci Rep* **6**, 28489 (2016).

79. H. T. Malloy, K. A. Evelyn, THE DETERMINATION OF BILIRUBIN WITH THE PHOTOELECTRIC COLORIMETER. *Journal of Biological Chemistry* **119**, 481-490 (1937).

80. L. Lobo *et al.*, New endoperoxides highly active in vivo and in vitro against artemisinin-resistant Plasmodium falciparum. *Malar J* **17**, 145 (2018).

81. S. A. Santos *et al.*, Exploring the 3-piperidin-4-yl-1H-indole scaffold as a novel antimalarial chemotype. *European journal of medicinal chemistry* **102**, 320-333 (2015).

82. A. Butler, P. Hoffman, P. Smibert, E. Papalexi, R. Satija, Integrating single-cell transcriptomic data across different conditions, technologies, and species. *Nat Biotechnol* **36**, 411-420 (2018).

83. Y. Hao *et al.*, Integrated analysis of multimodal single-cell data. *bioRxiv*, 2020.2010.2012.335331 (2020).

84. R. Satija, J. A. Farrell, D. Gennert, A. F. Schier, A. Regev, Spatial reconstruction of single-cell gene expression data. *Nat Biotechnol* **33**, 495-502 (2015).

85. D. J. McCarthy, K. R. Campbell, A. T. Lun, Q. F. Wills, Scater: pre-processing, quality control, normalization and visualization of single-cell RNA-seq data in R. *Bioinformatics* **33**, 1179-1186 (2017).

86. S. K. Dogga *et al.*, A single cell atlas of sexual development in Plasmodium falciparum. *bioRxiv* (2023).

87. V. Y. Kiselev, A. Yiu, M. Hemberg, scmap: projection of single-cell RNA-seq data across data sets. *Nat Methods* **15**, 359-362 (2018).

88. A. T. Lun, D. J. McCarthy, J. C. Marioni, A step-by-step workflow for low-level analysis of single-cell RNA-seq data with Bioconductor. *F1000Research* **5**, 2122 (2016).

89. M. Andreatta, S. J. Carmona, STACAS: Sub-Type Anchor Correction for Alignment in Seurat to integrate single-cell RNA-seq data. *Bioinformatics* **37**, 882-884 (2021).

90. L. Kolberg, U. Raudvere, I. Kuzmin, J. Vilo, H. Peterson, gprofiler2 -- an R package for gene list functional enrichment analysis and namespace conversion toolset g:Profiler. *F1000Research* **9**, (2020).

91. R. C. Team. (2021).

92. G. La Manno *et al.*, RNA velocity of single cells. *Nature* **560**, 494-498 (2018).

93. V. Gorki, R. Singh, N. S. Walter, U. Bagai, D. B. Salunke, Synthesis and Evaluation of Antiplasmodial Efficacy of beta-Carboline Derivatives against Murine Malaria. *ACS Omega* **3**, 13200-13210 (2018).

94. R. H. Pek *et al.*, Hemozoin produced by mammals confers heme tolerance. *Elife* **8**, (2019).

95. K. K. Ncokazi, T. J. Egan, A colorimetric high-throughput beta-hematin inhibition screening assay for use in the search for antimalarial compounds. *Anal Biochem* **338**, 306-319 (2005).

96. H. Tsugawa *et al.*, MS-DIAL: data-independent MS/MS deconvolution for comprehensive metabolome analysis. *Nature Methods* **12**, 523-526 (2015).

97. B. Drotleff, M. Lämmerhofer, Guidelines for Selection of Internal Standard-Based Normalization Strategies in Untargeted Lipidomic Profiling by LC-HR-MS/MS. *Analytical Chemistry* **91**, 9836-9843 (2019).

98. S. Dekina, T. Alexandrov, B. Drotleff, EMBL-MCF 2.0: an LC-MS/MS method and corresponding library for high-confidence targeted and untargeted metabolomics using low-adsorption HILIC chromatography. *Metabolomics* **20**, 114 (2024).

99. A. Figueiredo *et al.* (GEO: GSE254821, 2025).

100. A. Figueiredo *et al.* (Metabolomics Workbench; PR002327; doi:10.21228/M8V24V, 2025).

Acknowledgments

The authors are indebted to all members of the Inflammation laboratory (GIMM) for insightful technical and intellectual contributions, GIMM flow cytometry and animal facility. The authors thank DR de Waart (University of Amsterdam) for quantification of unconjugated bilirubin by HPLC (not shown), Akhil Vaidya (Drexel University, USA) for kindly providing the *Pf*D10 and *Pf*D10^{TgDHODH} strains and for insightful advice, the Centre de Recherches Médicales de Lambaréné for support of the DEMIT study, Lara Bardtke, Paolo Kroneberg, Anna Karolina Kneller, Nathalie Schirra, Johanna Lioba Schöllgen, and Claudia Conrad for sample and data processing at Charité - Universitätsmedizin Berlin, Oleg Chertkov (Católica Biomedical Research Centre, Portugal), Protein Purification Research Facility and the Bacterial Imaging Cluster at ITQB NOVA for support for protein purification and quantification, and Ana Malheiro (Advanced Electron Microscopy, Imaging and Spectroscopy – AEMIS) use of the INL User Facilities.

Funding

This work was supported by Fundação para a Ciência e Tecnologia (2020.04797.BD and COVID/BD/153665/2024 to AF; GHTMUID/04413/2020, LA-REAL-LA/P/0117/2020 and 2022.02426.PTDC to FN; FEDER/29411/2017 to SR; 2020.04797.BD to DD; UIDB/04565/2020, LA/P/0140/2020 and 2022.03627.PTDC to SP; 2022.08590.PTDC_EXPL DOI 10.54499/2022.08590.PTDC to JK; 2021.03494.CEECIND DOI 10.54499/2021.03494.CEECIND/CP1674/CT0004 to RM; 2023.09168.CEECID to EJ; FEDER/29411/2017, PTDC/MED-FSL/4681/2020 DOI 10.54499/PTDC/MED-FSL/4681/2020,

2022.02426.PTDC DOI 10.54499/2022.02426.PTDC and Congento LISBOA-01-0145-FEDER-022170 to MPS).

European Union's Horizon 2020 research and innovation programme under the Marie Skłodowska-Curie (955321 to AGGS,753236 to RM).

DFG Cluster of Excellence ‘‘Balance of the Microverse’’ EXC 2051; 390713860 (EJ, MPS as associated member). DFG IRTG 2290 “Molecular interactions in malaria” (P.T.L., F.K. and the DEMIT study).

Gulbenkian Foundation (SR, MPS and IBB 2021-51/BI-D/2021 to ST).

la Caixa Foundation HR18-00502 (EJ, JK, MPS).

Human Frontier Science Program (LT0043/2022-L to JK).

Lise Meitner Excellence Programme of the Max Planck Society (SP).

European Molecular Biology Organization (EMBO Long-term Fellowship ALTF290-2017 to RM).

European Union's Horizon 2020 research and innovation programme (Grant 955321).

Academy of Finland (Grant 329278 to LLE).

Sigrid Juselius Foundation (LLE).

Biocenter Finland (LLE).

ELIXIR Finland (LLE).

American Heart Association/Paul Allen Frontiers Group (Project 19PABH134580006 to BDP).

NIH/NIA (BDP by 1R21AG073684-01, R01AG071512).

The Johns Hopkins Catalyst Award (BDP).

Solve ME/CFS Initiative (Grant 90089823 to BDP).

US Public Health Service (Grant DA044123 to BDP).

European Research Council (Grant 101001521 to MJA).

Oeiras-ERC Frontier Research Incentive Awards (MPS).

H2020-WIDESPREAD-2020-5-952537 SymbNET Research Grants (MPS)

Author Contributions

Conceptualization: MPS, AF, RM, KV, SP

Data curation: AGGS, SJ, LVN, CW, PTL, FK, SV, TP, BD

Formal analysis: AGGS, SJ, LVN, CW, PTL, FK, SV, TP, BD

Resources: GMN, JN, CW, PTL, FK, BP, MJA, GB, AFM

Investigation: AF, SR, EJ, JT, DD, ALS, SP, SPa, STR, MM, SC, MA, JK, GMN, JM, CW, PTL, FK, MA, CC, RM

Visualization: AF, RM, MPS

Funding acquisition: MPS, RM, FK

Project administration: MPS, RM

Supervision: MPS, RM, FN, SJ, LLE, SNP, SP, JK, PJB, FK, ET, KV

Writing – original draft: MPS

Writing – review & editing: MPS, AF, RM, STR, SR

Competing interests

The authors declare that they have no competing interests. Chirag Vasavda is an inventor on patent US11442059 held by The Johns Hopkins University that covers Method for treating a chronic itch condition by administering small molecule MrgprX4 antagonists and on patent application US Patent App. 18/726,735 submitted by The Johns Hopkins University that covers Treatment and prevention of trigeminal neuralgia.

Data availability

All data are available in the main text or the supplementary materials. Clinical patient data is available from Florian Kurth (florian.kurth@charite.de) upon request. Single-cell RNAseq data are available in Gene Expression Omnibus (*99*) (accession number GSE254821) and Metabolomics data are available in (*100*).

Supplementary Materials

Figs S1–S20

Data tables S1–S5

Data S1–S3

Figure legends

Figure 1. **Unconjugated bilirubin confers resistance to malaria.** (**A**) Parasite burden (*P. falciparum* iRBC/μL of blood) and concentrations of (**B**) total (i.e., conjugated plus unconjugated), (**C**) conjugated and (**D**) unconjugated bilirubin (measured using the Roche Diazo method) in plasma from *P. falciparum* infected individuals, stratified according to disease severity as: asymptomatic and symptomatic malaria. (**E**) Plasma concentration of unconjugated bilirubin measured by the UnaG-based assay in same patients as (A-D). **(F)** Ratio of unconjugated bilirubin measured by the UnaG-based assay (E) to conjugated bilirubin (C). Data (A-F) is represented as box plots; red lines correspond to median values and error bars correspond to the interquartile range (IQR). (**G**) Concentration of unconjugated bilirubin in plasma from *Blvra*$^{+/+}$ and *Blvra*$^{-/-}$ mice (n=6-9 *per* genotype), before (Day 0) and after *Pcc* infection (Days 4, 7, 15 and 25) measured by the UnaG-based assay. Data represented as mean ± SD, pooled from two independent experiments with similar trend. (**H**) Survival of *Pcc*-infected *Blvra*$^{-/-}$ and control *Blvra*$^{+/+}$ mice. Data from n=7 *per* genotype, pooled from two independent experiments with similar trend. (**I**) Survival of *Pcc*-infected *Blvra*$^{-/-}$ mice receiving bilirubin (30 or 3 mg/Kg; daily; *i.p.*) or vehicle. Data from n=4-10 *per* treatment, pooled from two independent experiments with similar trend. (**J**) Quantification of *Ugt1a1* mRNA (qPCR; *left panel*) (n=7-9 *per* genotype) and protein (Western Blot; *right panel*) (n=6 *per* genotype) expression in the liver at day 7 post-*Pcc* infection (*Pcc*) or non-infected (NI) C57BL/6J mice. Data represented as mean ± SD, pooled from two independent experiments with similar trend. (**K**) Concentration of unconjugated bilirubin in plasma of adult DBA/2 mice transduced 2-4 days after birth with AAV8-gRNA-*Ugt1a1* repressing hepatic *Ugt1a1* or control AAV8-Cas9. Data from n=5 mice *per* group, represented as mean ± SD, from one experiment representative of three with similar trend. (**L**) Survival of the mice from (K) infected with *Pcc*. Circles in (A-F)

correspond to *P. falciparum*-infected patients and in (G-L) to individual mice. *P* values determined using: (A-F) Mann-Whitney U test, (G) Two-Way ANOVA with Bonferroni's multiple comparison test (for genotypes) and Ordinary One-Way ANOVA with Tukey's multiple comparison (for days post-infection), (H, I, L) Log-rank (Mantel-Cox) test, (J *right panel*, K) t test, and (J *left panel*) using Mann-Whitney U test. NS: not significant; *$p<0.05$; **$p<0.01$; ***$p<0.001$.

Figure 2. **Unconjugated bilirubin regulates *Plasmodium* blood stage development and virulence.** (**A**) Percentage of iRBC and (**B**) parasite burden (iRBC/µL) in *Pcc*-infected *Blvra*$^{-/-}$ and control *Blvra*$^{+/+}$ mice. Data from n=7 *per* genotype, pooled from two independent experiments with similar trend. Same mice as (Figure 1H). *Right panel* highlights Day 8 from *left panel*. (**C**) UMAP projection of single parasite transcriptomes, of FACS-sorted circulating iRBC from *Blvra*$^{+/+}$ (n= 1862; *left panel*) and *Blvra*$^{-/-}$ (n= 3891; *right panel*) mice, 7 days after *Pcc* infection. Colors and numbers identify different parasite developmental stages based on scmap projection to a *P. falciparum* atlas (*See Data tables S1-4*). (**D**) Composition and (**E**) absolute number of parasite developmental stages. (**F**) UMAP projection as in (C) with arrows representing the relative change in transcriptional state based on RNA velocity analysis. (**G**) Survival of *Blvra*$^{-/-}$ mice infected with *Pcc* iRBC, isolated from *Blvra*$^{-/-}$ *vs.* *Blvra*$^{+/+}$ mice (n=10-11 *per* genotype). (**H**) Percentage of iRBC (*left panel*), and parasite burden (iRBC/µL, *right panel*) of the same mice as (G). Data represented as mean ± SD, pooled from three independent experiments with similar trend. Circles in (B, *right panel*) represent individual mice. *P* values determined using: (A,B *left panel*, H) Two-Way ANOVA, (B *right panel*) Mann Whitney U test, and (G) Log-rank (Mantel-Cox) test. *p<0.05; **p<0.01; ***p<0.001; ****p<0.0001.

Figure 3. **Bilirubin inhibits *P. falciparum* proliferation and disrupts its mitochondrion integrity and function.** (**A**) Bilirubin accumulation in *P. falciparum* 3D7 (*Pf*3D7) iRBC (trophozoites), 8 and 12h after exposure to unconjugated bilirubin (41 μM) or vehicle. Data represented as mean ± SD, from one experiment, with 5 technical replicates. (**B**) Percentage (*left panel*) of *Pf*3D7 iRBC, 24-72h after exposure of ring stages to increasing concentrations of unconjugated bilirubin. Data represented as mean ± SEM, pooled from six independent experiments with similar trend, with four technical replicates *per* experiment. *Right panel* is a representative Giemsa-stained thin smear, 24h after exposure to unconjugated bilirubin (41 μM) or vehicle. Black arrowhead highlights parasite nuclear DNA fragmentation. Scale bars: 2 μm. (**C**) Relative levels of Glucose, Glucose 6-phosphate, Succinate, Aspartate (Asp), Fumarate and Adenosine Monophosphate (AMP) in *Pf*3D7 iRBC (trophozoites), detected by Mass Spectrometry 12h after exposure to unconjugated bilirubin (41 μM) or vehicle. Data represented as mean ± SD, from one experiment, with 5 technical replicates (*See Data table S5*). (**D**) Schematic representation of differentially expressed genes involved in metabolic processes in *P. chabaudi chabaudi* iRBC isolated from *Blvra*$^{-/-}$ *vs. Blvra*$^{+/+}$ mice, as determined by scRNA sequencing, in the different clusters identified in (Fig. 2C-F). (**E**) Representative histograms (*left panel*) and quantification of median fluorescence intensity (MFI; *right panel*) of mitochondrion volume (MitoTracker Green), 24h after exposure of *Pf*3D7 iRBC (rings) to increasing concentrations of unconjugated bilirubin. Grey histogram represents background staining in non-infected RBC and dotted grey line (*right panel*) represents the average background signal from all replicates in non-infected RBC. Data represented as mean ± SD from four replicates in one out of two independent experiments with similar trend. (**F**) Relative level of dihydroorotate (DHO, *left panel*), orotate (*middle panel*) and uridine monophosphate (UMP, *right panel*), in *Pf*3D7-iRBC (trophozoites), detected by Mass Spectrometry 12h after exposure to unconjugated

bilirubin (41 μM) or vehicle. (*See Data table S5*). (**G**) Percentage (*left panel*) of *Pf*D10^{TgDHODH} iRBC (*P. falciparum* D10 transgenic strain expressing a cytoplasmic *Saccharomyces cerevisiae* DHODH) (rings), after exposure to increasing concentrations of unconjugated bilirubin. Data represented as mean ± SEM, pooled from 3 independent experiments with similar trend, with four biological replicates *per* experiment. *Right panel* is representative Giemsa-stained thin smears, 24h after exposure to unconjugated bilirubin (41 μM) or vehicle. Black arrowhead highlights pyknotic parasites. Scale bars: 2μm. Dots in (A,E,F) represent technical replicates and in (C) individual mice. *P* values determined using: (A, E) Ordinary One-Way ANOVA with Tukey's multiple comparison test, (B, G) Two Way ANOVA with Tukey's multiple comparison test, and (C, F) Mann Whitney U test. *p<0.05; **p<0.01; ***p<0.001; ****p<0.0001. Concentration of unconjugated bilirubin in (A,B,C,E,F,G) were calculated according to the UnaG-based assay (*21, 22*) (*see Fig. S10*).

Figure 4. **Bilirubin inhibits Hz formation and disrupts *P. falciparum* food vacuole.** (**A**) Live confocal microscopy of *Pf*3D7 iRBC (trophozoites), 12h after exposure to unconjugated bilirubin (41 μM) or vehicle. Representative images (*left panel*) and quantification of Hz cellular intensity distribution (laser reflection mode, cyan; area, *right panel*). RBC membranes stained with wheat germ agglutinin (RBC; red), and nuclei (N) with Hoechst (DNA: blue). Data in *right panel* represented as mean ± SD from two independent experiments (n=10-15 parasites). Scale bars: 4 μm. (**B**) Relative inhibition of β-hematin crystallization by bilirubin *vs.* chloroquine. Equimolar amounts of Brivanib alaninate (a tyrosine kinase inhibitor) were used as control. The relative inhibition of β-hematin crystallization was inferred from heme accumulation measured at λ_{405} nm (*95*) and is represented as the mean of λ/λ_{405} nm ± SD from two replicates in one out of two independent experiments with similar trend. (**C**) Hz quantification in blood from *Blvra*$^{+/+}$ and *Blvra*$^{-/-}$ 7 days after *Pcc* infection, at daily light (*left panel*) and dark (*right panel*) cycle. Hz (*i.e.*, nM heme), represented as mean ± SD, pooled from two independent experiments with similar trend (n=11; light cycle and n=9-10; dark cycle; *per* genotype). (**D**) Representative images (*left panel*) and quantification (*right panel*) of food vacuole (Area under the curve; AUC). RBC membranes stained with wheat germ agglutinin (RBC; red), parasite´s food vacuole (FV) with LysoTracker Green (green) and nuclei (N) with Hoechst (DNA: blue). Data in *right panel* represented as mean ± SD from two independent experiment (n=10-13 parasites), as in (A). Scale bars: 4 μm. (**E**) Representative transmission electron microscopy images of *Pf*3D7 iRBC (trophozoites), 12h after exposure to unconjugated bilirubin (41 μM) or vehicle. *Right panel* correspond to amplifications of the orange dotted area highlighted in *left panel*. EV: Endocytic vesicle, FV: Food vacuole, Hz: Hemozoin, MLB: Multilamellar bodies, N: Nucleus, RBC: Red blood cell. Images are representative of three independent experiments with similar results. Scale bars: 500 nm. (**F**) Relative levels of amino acids in *Pf*3D7-iRBC (trophozoites) (Leucine (Leu),

Phenylalanine (Phe), Valine (Val), Threonine (Thr), Tryptophan (Trp), Lysine (Lys), Proline (Pro), Methionine (Met) and Isoleucine (Ile)) as detected by Mass Spectrometry, 12h after exposure to unconjugated bilirubin (41 μM) or vehicle (*See Data table S5*). Circles in (A,D) represent individual parasite, in (C) individual mice and (F) technical replicates. *P* values determined using: (A, C, D, F) Mann-Whitney U test. NS: not significant; *p<0.05, **p<0.01; ****p<0.0001. Concentration of unconjugated bilirubin in (A,B,C,E,F,G) were calculated according to the UnaG-based assay (*21, 22*) (*see Fig. S10*).

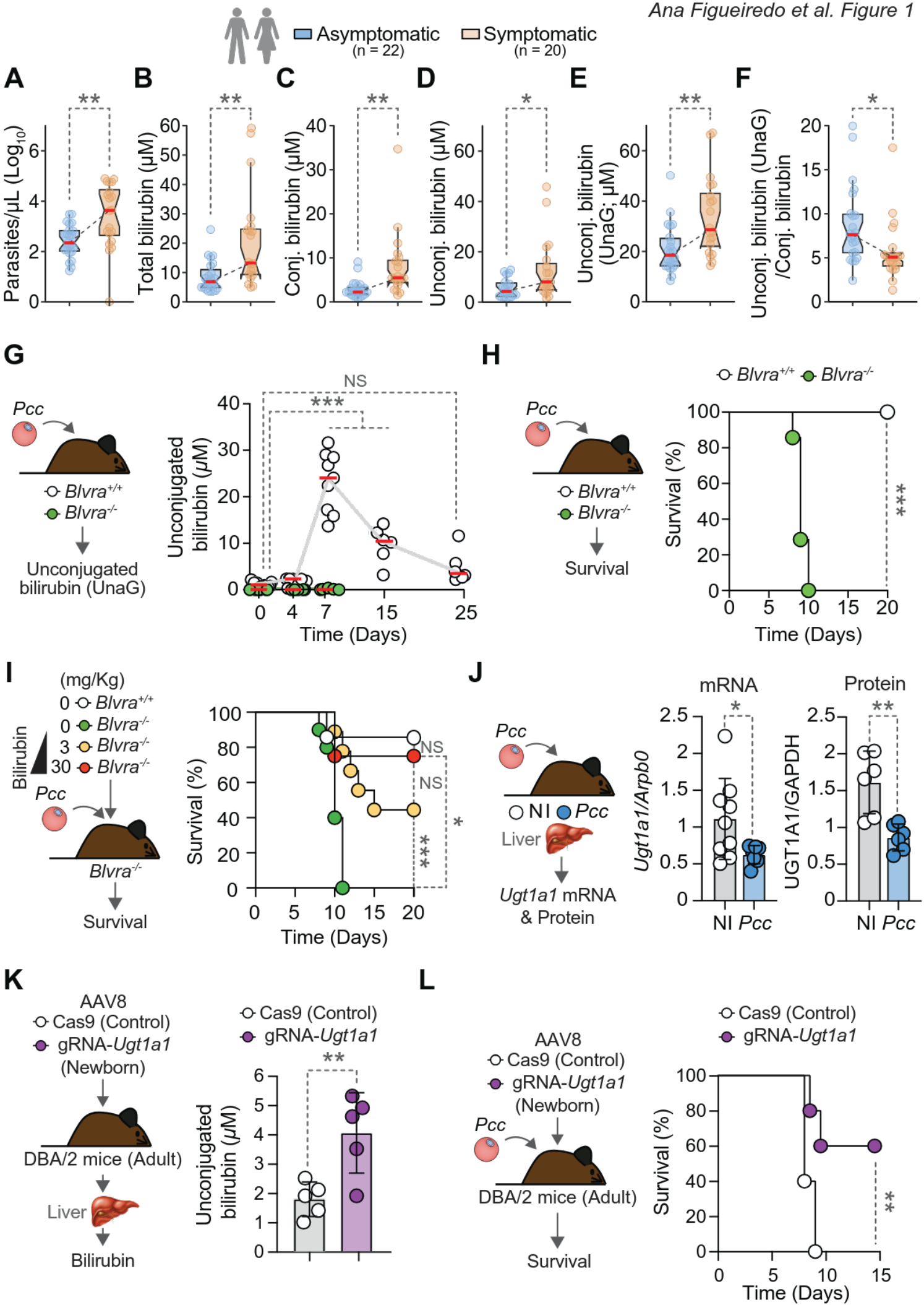
Asymptomatic (n = 22)
Symptomatic (n = 20)
A
Parasites/µL (Log10)
B
Total bilirubin (µM)
C
Conj. bilirubin (µM)
D
Unconj. bilirubin (µM)
E
Unconj. bilirubin (UnaG; µM)
F
Unconj. bilirubin (UnaG) /Conj. bilirubin
G
Pcc
Blvra+/+
Blvra-/-
Unconjugated bilirubin (UnaG)
Unconjugated bilirubin (µM)
NS
***
Time (Days)
H
Survival
Survival (%)
I
(mg/Kg)
0 Blvra+/+
0 Blvra-/-
3 Blvra-/-
30 Blvra-/-
Bilirubin
J
NI Pcc
Liver
Ugt1a1 mRNA & Protein
mRNA
Protein
Ugt1a1/Arpb0
UGT1A1/GAPDH
K
AAV8
Cas9 (Control)
gRNA-Ugt1a1
(Newborn)
DBA/2 mice (Adult)
Bilirubin
L

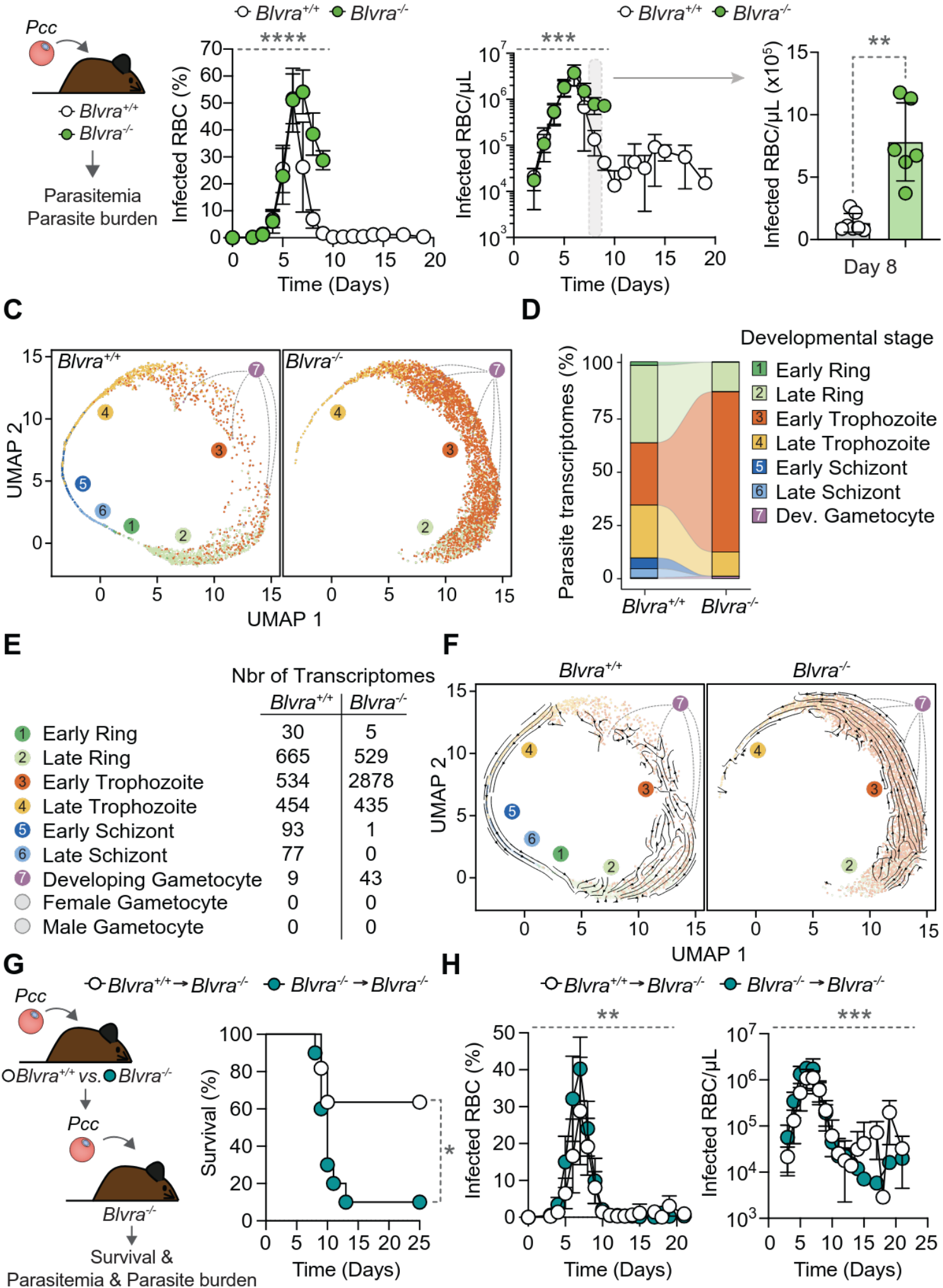
A
Pcc
Blvra+/+
Blvra-/-
Parasitemia
Parasite burden
Blvra+/+ Blvra-/-
****
Infected RBC (%)
Time (Days)
B
Blvra+/+ Blvra-/-
***
Infected RBC/µL
Time (Days)
**
Infected RBC/µL (x10^5)
Day 8
C
Blvra+/+
Blvra-/-
UMAP 2
UMAP 1
D
Developmental stage
1 Early Ring
2 Late Ring
3 Early Trophozoite
4 Late Trophozoite
5 Early Schizont
6 Late Schizont
7 Dev. Gametocyte
Parasite transcriptomes (%)
Blvra+/+
Blvra-/-
E
Nbr of Transcriptomes
Blvra+/+ | Blvra-/-
1 Early Ring 30 | 5
2 Late Ring 665 | 529
3 Early Trophozoite 534 | 2878
4 Late Trophozoite 454 | 435
5 Early Schizont 93 | 1
6 Late Schizont 77 | 0
7 Developing Gametocyte 9 | 43
Female Gametocyte 0 | 0
Male Gametocyte 0 | 0
F
Blvra+/+
Blvra-/-
UMAP 2
UMAP 1
G
Blvra+/+→Blvra-/-
Blvra-/-→Blvra-/-
Pcc
Blvra+/+ vs. Blvra-/-
Pcc
Blvra-/-
Survival &
Parasitemia & Parasite burden
Survival (%)
*
Time (Days)
H
Blvra+/+→Blvra-/-
Blvra-/-→Blvra-/-
**
Infected RBC (%)
Time (Days)
***
Infected RBC/µL
Time (Days)

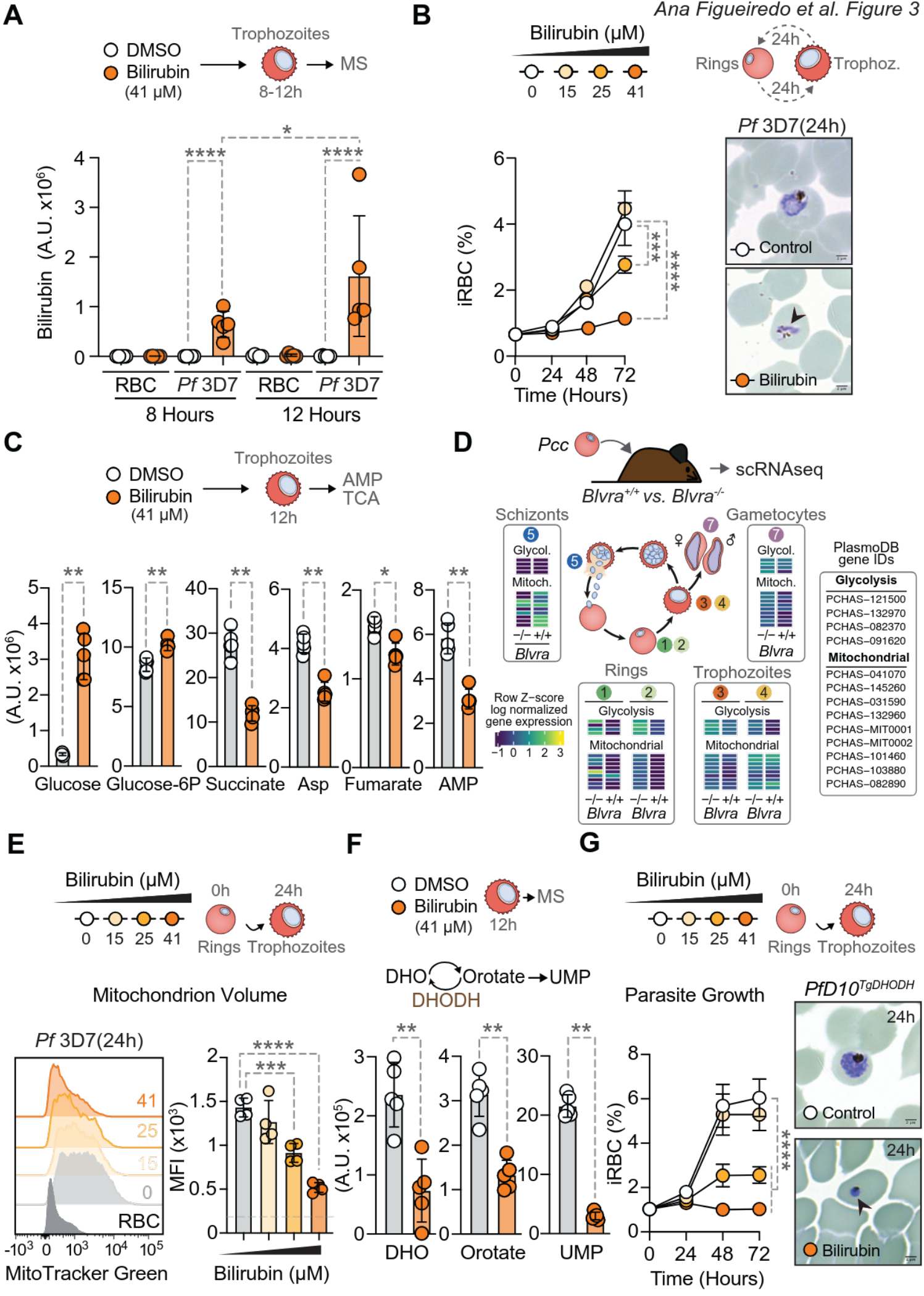
A
DMSO
Bilirubin
(41 µM)
Trophozoites
8-12h
MS
Bilirubin (A.U. x10^6)
RBC
Pf 3D7
RBC
Pf 3D7
8 Hours
12 Hours
B
Bilirubin (µM)
0 15 25 41
24h
Rings
Trophoz.
24h
Pf 3D7(24h)
iRBC (%)
Time (Hours)
Control
Bilirubin
C
DMSO
Bilirubin
(41 µM)
Trophozoites
12h
AMP
TCA
(A.U. x10^6)
Glucose
Glucose-6P
Succinate
Asp
Fumarate
AMP
D
Pcc
scRNAseq
Blvra+/+ vs. Blvra-/-
Schizonts
Gametocytes
Glycol.
Mitoch.
−/− +/+
Blvra
Rings
Trophozoites
Glycolysis
Mitochondrial
Row Z-score
log normalized
gene expression
PlasmoDB
gene IDs
Glycolysis
PCHAS−121500
PCHAS−132970
PCHAS−082370
PCHAS−091620
Mitochondrial
PCHAS−041070
PCHAS−145260
PCHAS−031590
PCHAS−132960
PCHAS−MIT0001
PCHAS−MIT0002
PCHAS−101460
PCHAS−103880
PCHAS−082890
E
Bilirubin (µM)
0 15 25 41
0h
24h
Rings
Trophozoites
Mitochondrion Volume
Pf 3D7(24h)
MFI (x10^3)
MitoTracker Green
Bilirubin (µM)
F
DMSO
Bilirubin
(41 µM)
MS
12h
DHO
Orotate
UMP
DHODH
(A.U. x10^5)
G
Bilirubin (µM)
0 15 25 41
0h
24h
Rings
Trophozoites
Parasite Growth
PfD10TgDHODH
iRBC (%)
Time (Hours)
Control
Bilirubin

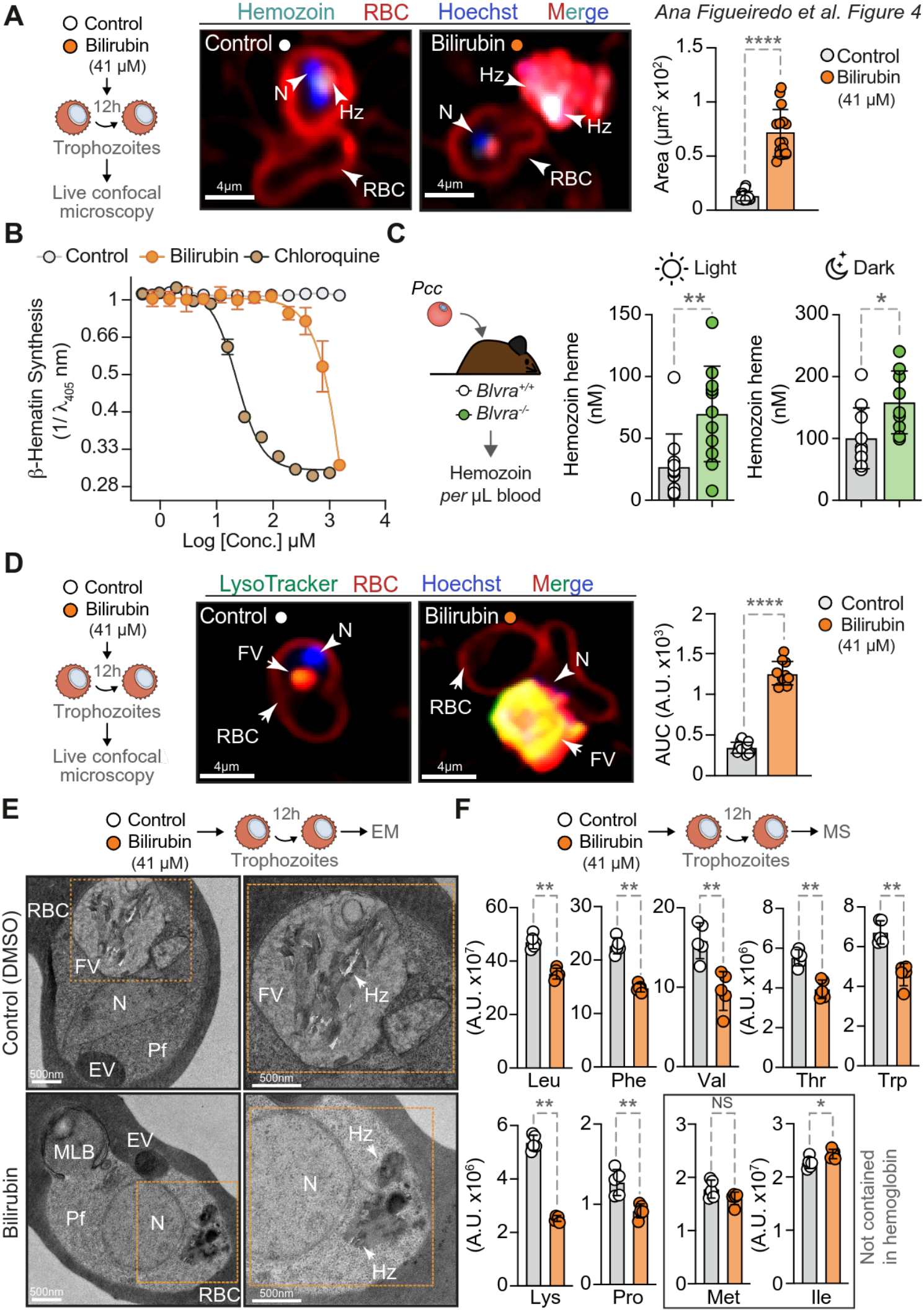
A
Control
Bilirubin
(41 μM)
12h
Trophozoites
Live confocal microscopy
Hemozoin
RBC
Hoechst
Merge
Control
Bilirubin
N
Hz
RBC
4μm
Area (μm² x10²)
****
B
Control
Bilirubin
Chloroquine
β-Hematin Synthesis (1/ λ405 nm)
Log [Conc.] μM
C
Pcc
Blvra+/+
Blvra-/-
Hemozoin per μL blood
Light
Dark
Hemozoin heme (nM)
**
*
D
LysoTracker
RBC
Hoechst
Merge
FV
AUC (A.U. x10³)
E
EM
Control (DMSO)
Bilirubin
MLB
EV
Pf
F
MS
(A.U. x10⁷)
(A.U. x10⁶)
Leu
Phe
Val
Thr
Trp
Lys
Pro
Met
Ile
NS
Not contained in hemoglobin